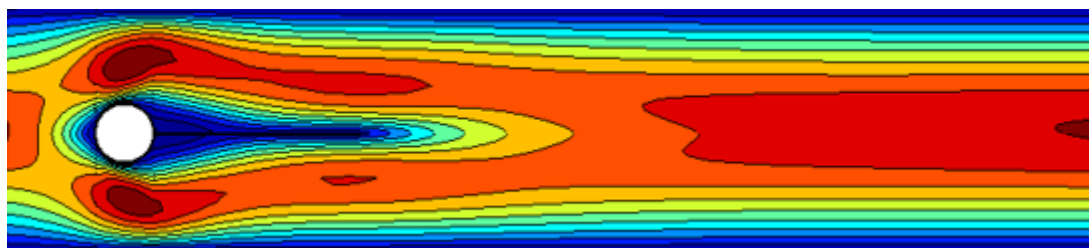


Gonzalo Carrasco García

# Investigation of a Fluid-Structure Interaction Method for a Flexible Plate in Viscous Compressible Channel Flow

Trondheim, June 2016

NTNU  
Norwegian University of  
Science and Technology  
Faculty of Engineering Science and Technology  
Department of Energy and Process Engineering



**PROJECT WORK**

for

Student Gonzalo Carrasco

Spring 2016

**Investigation of a Fluid-Structure Interaction Method for a Flexible Plate in  
Viscous Compressible Channel Flow**

*Undersøkelse av en fluid-struktur interaksjonsmetode for en fleksibel plate i  
viskøs kompressibel kanalstrømning*

**Background and objective**

Flapping of a flag is a classical example of the interaction of the wind and the elastic structure of a flag. The prediction of flapping motion is not only important for flapping flags, but also for flutter of wings and sails as well as understanding the swimming of fish. Another example of fluid-structure interacting (FSI) is the flapping motion of the soft palate in the human pharynx. During sleep, the soft palate can make contact with the pharynx wall and lead to the obstructive sleep apnea syndrome (OSAS). Because of its great importance for public health, OSAS has been investigated in a larger research project entitled Modeling of obstructive sleep apnea by fluid-structure interaction in the upper airways (OSAS Mod), which has been funded by the Research Council of Norway. In the OSAS Mod research project, an FSI method has been developed based on an Arbitrary Lagrangian-Eulerian approach, in which the compressible Navier-Stokes equations are solved by a fourth order finite difference method and the thin plate equations by the Newmark method. Since the specialization project will be associated with the OSAS Mod research project, the student will be a member of the international OSAS Mod team.

The objective of the specialization project is to validate an existing method for FSI between viscous compressible channel flow and a flexible plate modeling FSI of the soft palate in the human pharynx by comparison with an FSI experiment.

**The following tasks are to be considered:**

1. to get a basic physical understanding of FSI, its mathematical description and its numerical solution,
2. to validate the FSI method by comparison with an FSI experiment,
3. to point out strengths and improvements of the FSI method.

-- " --

The project work comprises 15 ECTS credits.

The work shall be edited as a scientific report, including a table of contents, a summary in Norwegian, conclusion, an index of literature etc. When writing the report, the candidate must emphasise a clearly arranged and well-written text. To facilitate the reading of the report, it is important that references for corresponding text, tables and figures are clearly stated both places. By the evaluation of the work the following will be greatly emphasised: The results should be thoroughly treated, presented in clearly arranged tables and/or graphics and discussed in detail.

The candidate is responsible for keeping contact with the subject teacher and teaching supervisors.

Risk assessment of the candidate's work shall be carried out according to the department's procedures. The risk assessment must be documented and included as part of the final report. Events related to the candidate's work adversely affecting the health, safety or security, must be documented and included as part of the final report. If the documentation on risk assessment represents a large number of pages, the full version is to be submitted electronically to the supervisor and an excerpt is included in the report.

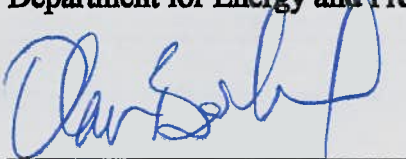
According to "Utfyllende regler til studieforskriften for teknologistudiet/sivilingeniørstudiet ved NTNU" § 20, the Department of Energy and Process Engineering reserves all rights to use the results and data for lectures, research and future publications.

The report shall be submitted to the department in 3 complete, bound copies.

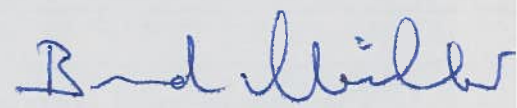
Submission deadline: June 10, 2016.

- Work to be done in lab (Water power lab, Fluids engineering lab, Thermal engineering lab)  
 Field work

Department for Energy and Process Engineering, 25 January 2016.



Olav Bolland  
Department Head



Bernhard Müller  
Supervisor

## **Abstract**

This report presents a detailed investigation of a method for fluid-structure interaction (FSI) between a flexible plate and viscous compressible channel flow. The FSI of a simplified two-dimensional model of the soft palate in the human pharynx is considered. Based on an arbitrary Lagrangian-Eulerian approach, it uses a high order finite difference method relying on summation by parts operators in space and a fourth-order explicit Runge-Kutta method in time for the discretization of the compressible Navier-Stokes equations. A multi-block division of the computational domain, together with the use of message passing interface, enables a parallel solution of the flow field. The motion of the structure is modeled by the classical thin-plate mechanics governed by the Euler-Bernoulli beam model equations that are solved by the Newmark method. By comparison with a FSI experiment, the fluid and structure solvers are tested separately aiming to prove the correct performance of each of them, needed to accomplish the full validation of the whole FSI method.

# Preface

The following report documents the project work carried out during the spring semester of 2016 in the Department of Energy and Process Engineering at the Norwegian University of Science and Technology. It is the final result of the course “TEP4540 Engineering Fluid Mechanics, Specialization Project” which comprises a total amount of 15 ECTS credits. This specialization project is associated with the larger research project entitled “Modeling of Obstructive Sleep Apnea by Fluid-Structure Interaction in the Upper Airways (OSAS Mod)” [1], which has been funded by the Research Council of Norway.

I would like to give special thanks to Bernhard Müller for his guidance and support as a supervisor, and for increasing my interest in Computational Fluid Dynamics as a professor.

The code and advice given by Ehsan Khalili were really appreciated and helpful for a better understanding of the method.

Finally I would like to thank the rest of the members of the international OSAS Mod team for making me feel as part of the project from the very first minute.

Gonzalo Carrasco García

Trondheim, 29<sup>th</sup> May 2016

# Table of Contents

<b>Abstract .....</b>	<b>i</b>
<b>Preface.....</b>	<b>ii</b>
<b>List of tables.....</b>	<b>v</b>
<b>List of figures.....</b>	<b>vi</b>
<b>List of symbols.....</b>	<b>viii</b>
<b>List of abbreviations .....</b>	<b>x</b>
<b>1. Introduction .....</b>	<b>1</b>
1.1. FSI background.....	1
1.2. Motivation .....	1
<b>2. Mathematical description.....</b>	<b>3</b>
2.1. Fluid .....	3
2.2. Structure .....	5
2.3. Fluid-structure interaction.....	6
2.4. FSI benchmark.....	8
2.5. Initial and boundary conditions .....	12
2.6. Non-dimensional perturbation form .....	14
<b>3. Numerical models .....</b>	<b>15</b>
3.1. Fluid .....	16
3.2. Structure .....	19
3.3. Fluid-structure interaction.....	21
<b>4. Results .....</b>	<b>22</b>
4.1. CSM Tests.....	24
4.1.1. CSM3 .....	25
4.1.2. CSM1 .....	34
4.1.3. CSM2 .....	36
4.2. CFD Tests.....	37
4.2.1. CFD1.....	39
4.2.2. CFD2.....	47
4.2.3. CFD3 .....	49
4.3. FSI Tests .....	50
<b>5. Conclusions and outlook.....</b>	<b>52</b>

5.1. Conclusions .....	52
5.2. Outlook .....	52
<b>References .....</b>	<b>54</b>

# List of tables

2.1. Overview of test case geometry parameters .....	9
2.2. Overview of fluid material parameters .....	10
2.3. Overview of solid material parameters .....	11
4.1. Grid refinement levels from the FSI benchmark .....	23
4.2. Overview of parameters for structural tests .....	24
4.3. Input parameters for structural tests .....	25
4.4. CSM3 results: Time step and grid refinement studies .....	32
4.5. CSM3: Relative error of the results .....	34
4.6. CSM1 results: Grid refinement study .....	35
4.7. CSM1: Relative error of the results .....	35
4.8. CSM2 results: Grid refinement study .....	36
4.9. CSM2: Relative error of the results .....	37
4.10. Parameter setting for the CFD tests .....	38
4.11. CFD1: Reference results .....	39
4.12. CFD1: Non-dimensional reference results .....	40
4.13. CFD1: Time step influence .....	46
4.14. CFD2: Reference results .....	48
4.15. CFD2: Non-dimensional reference results .....	48
4.16. CFD2: Numerical results .....	49
4.17. CFD3: Reference results for $\Delta t=0.01$ s and $\Delta t=0.005$ s .....	49
4.18. Parameter setting for the FSI tests.....	51

# List of figures

1.1. Schematic of the human upper airways .....	2
2.1. Control volume .....	3
2.2. Test case computational domain .....	9
2.3. Detail of the structural part .....	9
2.4. Integration path for the force calculation .....	11
3.1. Original computational domain for the case in the upper airways .....	16
3.2. Schematic of the block structure for the FSI experiment .....	17
3.3. Schematic of points overlapping along a line .....	17
3.4. Computational domain for the simulations .....	18
3.5. Detail of the structure in the computational domain .....	19
3.6. Schematic of the FSI algorithm of the method .....	22
4.1. Example of a coarse mesh from the FSI benchmark .....	23
4.2. CSM3 Displacement of the whole structure .....	26
4.3. CSM3 Displacement of the whole structure: First oscillation .....	26
4.4. CSM3: $\Delta t = 0.02$ s. Coarse grid .....	27
4.5. CSM3: $\Delta t = 0.02$ s. Medium grid .....	28
4.6. CSM3: $\Delta t = 0.02$ s. Fine grid .....	28
4.7. CSM3: $\Delta t = 0.01$ s. Coarse grid .....	29
4.8. CSM3: $\Delta t = 0.01$ s. Medium grid .....	29
4.9. CSM3: $\Delta t = 0.01$ s. Fine grid .....	30
4.10. CSM3: $\Delta t = 0.005$ s. Coarse grid .....	30
4.11. CSM3: $\Delta t = 0.005$ s. Medium grid .....	31
4.12. CSM3: $\Delta t = 0.005$ s. Fine grid .....	31
4.13. First oscillations of CSM3: $\Delta t = 0.005$ s. Fine grid .....	33
4.14. CFD1: Convergence of the solution. Equidistant grid .....	40
4.15. Detail of the values for $\Delta pE$ surrounding the structure .....	41
4.16. Computational domain for clustered grid .....	42
4.17. CFD1: Clustered grid .....	43

4.18. CFD1: Pressure distribution .....	44
4.19. CFD1: Pressure profile along the cylinder surface .....	44
4.20. CFD1: Horizontal velocity distribution .....	45
4.21. CFD1: Vorticity distribution .....	45
4.22. Computational domain using refined grid clustering .....	47
4.23. CFD2: Clustered grid .....	48
4.24. CFD3: Clustered grid .....	50

## List of symbols:

*In order of appearance:*

$\Omega$ : Control volume

$\delta\Omega$ : Boundary of the control volume

$\mathbf{n}$ : Outer unit normal vector

$t$ : Time

$\rho$ : Density

$\mathbf{u}$ : Velocity vector

$p$ : Pressure

$\boldsymbol{\tau}$ : Viscous stress tensor

$E$ : Total energy per unit mass

$\mathbf{q}$ : Heat flux

$\mu$ : Dynamic viscosity

$\mathbf{U}$ : Conservative variables vector

$\mathbf{F}$ : Flux tensor

$\mathbf{F}^c$ : Inviscid normal flux vector

$\mathbf{F}^v$ : Viscous normal flux vector

$\mathbf{I}$ : Unit tensor

$k$ : Thermal conductivity

$T$ : Temperature

$e$ : Internal energy

$\gamma$ : Ratio of specific heats

$w$ : Vertical displacement of the structure

$p_u$ : Pressure on the upper surface of the structure

$p_l$ : Pressure on the lower surface of the structure

$M$ : Specific mass of the structure

$\rho^s$ : Density of the structure

$h$ : Thickness of the structure

$B$ : Flexural rigidity of the structure

$E^s$ : Young modulus of the structure

$\nu$ : Poisson ratio

C: Damping of the structure

$y_f$ : Vertical coordinate of the fluid grid point at the interface

$u^f$ : Horizontal velocity of the fluid

$\bar{U}$ : Mean inflow velocity

H: Height of the channel

L: Length of the channel

$p'$ : Gauge pressure

d: Diameter of the cylinder

$\nu^f$ : Kinematic viscosity of the fluid

$\rho_0$ : Stagnation density

$p_0$ : Stagnation pressure

J: Jacobian determinant of coordinate transformation

$\Delta x$ : Grid spacing in direction x

$\Delta y$ : Grid spacing in direction y

$\Delta t$ : Time step size

c: Speed of sound

g: Absolute value of the gravitational acceleration

L: Lift force

$C_L$ : Lift coefficient

D: Drag force

$C_D$ : Drag coefficient

$w_z$ : Z-component of vorticity vector

## List of abbreviations:

*In alphabetical order:*

ALE: Arbitrary Lagrangian-Eulerian

CFD: Computational Fluid Dynamics

CSM: Computational Structure Mechanics

FDM: Finite Difference Method

FSI: Fluid-Structure Interaction

GCL: Geometric Conservation Law

MPI: Message Passing Interface

OSAS: Obstructive Sleep Apnea Syndrome

OSAS Mod: Modeling of Obstructive Sleep Apnea by Fluid-Structure Interaction in the Upper Airways

SBP: Summation by parts

1D: One-dimensional

2D: Two-dimensional

# 1. Introduction

This section aims to give a general idea of the fluid-structure interaction concept and to show some real examples where FSI is present. In addition, the main reasons that motivate the specialization project are presented.

## 1.1. FSI background

The interaction between a deformable structure and a surrounding external or internal fluid flow is considered as one of the most important and complex multi-physics problems regarding its associated modeling and computational challenges [2].

Fluid-structure interaction is governed by the coupling between the physical laws describing both fluid dynamics and structural mechanics. The interactions which characterize this multi-physics phenomenon might be either stable or oscillatory.

If a body is submerged in a fluid flow, a cycled exchange of mechanical energy takes place between the fluid and the structure. The forces exerted by the fluid at the body surface cause the motion of the solid, which leads to a movement of the fluid-structure interface [3]. Depending on the flow and material properties, the deformations experienced by the structure can be small or large, leading to a bi-directionally coupled multi-physics problem. Moreover, for fast variations in time even small deformations generate pressure waves in the flow causing the typical sound of vibrating structures.

Even though FSI might not be noticed in everyday life, there is a wide range of cases where this phenomenon plays an important role: swimming of aquatic animals, mechanism of natural and artificial heart valves, flapping of a flag, movement of trees and plants in the wind, vocal folds in the larynx, liquids contained in flexible reservoirs, flow-induced vibrations on aeronautical and marine structures, performance of parachutes and airbags etc.

Therefore, the understanding of fluid-structure interaction can be truly helpful in completely different scenarios, from aero-elastic problems such as flutter of the wings of an aircraft to medical issues like aneurysms in large arteries.

## 1.2. Motivation

Among all the FSI cases that can be found in real life, this specialization project focuses on one in particular: Obstructive sleep apnea syndrome (OSAS).

OSAS is defined as an intrinsic sleep disorder characterized by repetitive episodes of paused breathing during sleep. It is caused by the complete or partial obstruction of the upper airways which leads to a reduction in blood oxygen saturation [4].

These obstructions are due to the relaxation of the muscles situated in the back of the throat, just at the entrance of the pharynx, where the narrowest part of the upper airways is located.

When a person is awake the muscles keep the airway open, while during sleep they relax narrowing the mentioned entrance. In that situation, the air passing through can give rise to vibrations of the soft palate causing snoring. But there are some cases where the throat closes so much that the quantity of air that enters the lungs is not enough. Therefore the brain has to re-activate the muscles to open the airway, which normally is associated with a brief interruption of sleep. This process can be better understood by looking at Figure 1.1 [5], where two pictures of the upper airways enable to see the differences between normal breathing and the case of blocked airways.

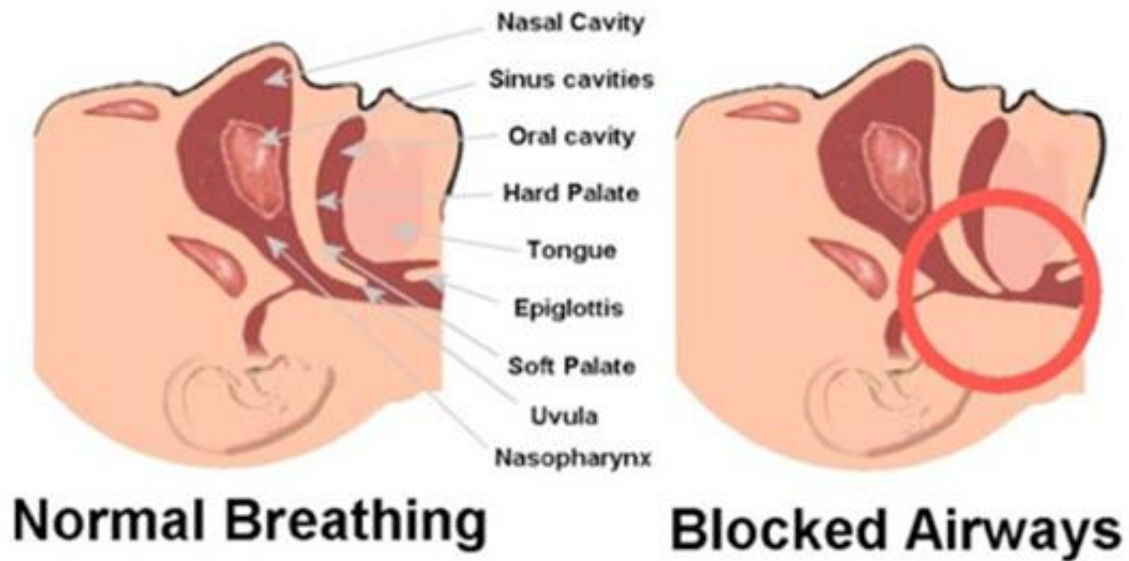


**Figure 1.1.** Schematic of the human upper airways

Since the soft tissues of the upper airways are flexible, the whole problem can be modeled by FSI between the soft palate and the air flowing through.

The prevalence of OSAS is estimated to be 2% for women and 4% for men [4]. This sleep disorder gives rise to low quality sleep and reduced oxygen consumption, which are some of the reasons why it is considered as a major cause for reduced life quality and increased mortality in nowadays society.

Due to its great importance for public health, OSAS is being investigated in a research project entitled “*Modeling of Obstructive Sleep Apnea by Fluid-Structure Interaction in the Upper Airways (OSAS Mod)*” [1]. This research project, which has been funded by the Research Council of Norway, aims to develop a clinical tool in order to be able to predict the responses of surgeries for OSAS patients and to identify the decisive pathophysiological mechanisms for the development of OSAS.

This specialization project is associated with the OSAS Mod research project, in particular with the work package called “*Mathematical Modeling of Fluid-Structure Interactions*”, which couples the compressible flow field in the pharynx to a model of the deformable structure in a two-way explicit form. For that purpose, a FSI method based on an arbitrary Lagrangian-

Eulerian (ALE) approach has been developed using a high order finite difference method (FDM) to solve the coupled fluid and structural problems [6].

In this context, the main objective of the specialization project is to validate the mentioned existing method for FSI between a flexible plate and viscous compressible channel flow by comparison with a FSI experiment. Therefore, it starts dealing with the theory behind FSI in section 2 and its numerical solution in section 3, to be able to understand the results obtained by numerical simulations in section 4, and compare them with those given as a reference in the FSI experiment.

## 2. Mathematical description

The purpose of this section is to set the general mathematical and physical basis for the entire project work.

Due to the complexity of the whole fluid-structure interaction problem, the theory of both fluid and structure is analyzed separately, to enable the study of all the relations and interactions between both of them later on.

After describing the governing equations for both fluid and structure and their interaction in the FSI method, the FSI experiment is presented in detail. According to the description of the test case, the initial and boundary conditions are defined in order to complete the mathematical description of the whole problem.

### 2.1. Fluid

The Navier-Stokes equations are derived from the conservation laws for mass, momentum and energy. Considering a compressible fluid flow, the resulting mixed hyperbolic-parabolic system of equations is known as the compressible Navier-Stokes equations [7] [8]. This system presents the governing equations for the case of study.

The control volume under consideration is denoted by  $\Omega$ , being time dependent and moving with the fluid flow.

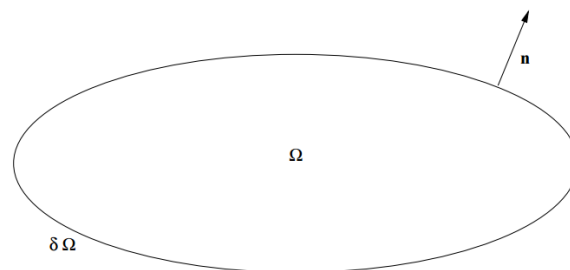


Figure 2.1. Control volume

In Figure 2.1 [7] the symbols  $\delta\Omega$  and  $\mathbf{n}$  refer to the boundary of the control volume and the outer unit normal vector, respectively.

The derivation of the conservation laws leads to the following three equations:

Continuity equation:

From the conservation law for mass, the total rate of mass change in  $\Omega$  is zero. The control volume is generally defined as time dependent, but the same equation applies for a stationary control volume [7].

$$\int_{\Omega} \frac{\partial \rho}{\partial t} dV + \int_{\partial\Omega} \rho \mathbf{u} \cdot \mathbf{n} dA = 0 \quad (2.1)$$

In (2.1), the symbols  $t$ ,  $\rho$  and  $\mathbf{u}$  are referring to the time, density and velocity vector of the fluid respectively.

Momentum equation:

From Newton's second law of motion, the total rate of momentum change in the control volume equals the sum of acting forces [7], which are in this case pressure and viscous forces, not taking into account volume forces such as gravity.

$$\int_{\Omega} \frac{\partial \rho \mathbf{u}}{\partial t} dV + \int_{\partial\Omega} \rho \mathbf{u} \mathbf{u} \cdot \mathbf{n} dA = - \int_{\partial\Omega} p \mathbf{n} dA + \int_{\partial\Omega} \boldsymbol{\tau} \cdot \mathbf{n} dA \quad (2.2)$$

Pressure is denoted by  $p$ , and  $\boldsymbol{\tau}$  is the viscous stress tensor in (2.2).

Energy equation:

From the first law of thermodynamics, the total rate of total energy change in  $\Omega$  equals the sum of the rate of heat added and the rate of work done on the fluid by the acting forces [7]. As in the momentum equation, the volume forces are not taken into account, so the acting forces are just pressure and viscous forces.

$$\int_{\Omega} \frac{\partial \rho E}{\partial t} dV + \int_{\partial\Omega} \rho E \mathbf{u} \cdot \mathbf{n} dA = - \int_{\partial\Omega} p \mathbf{u} \cdot \mathbf{n} dA + \int_{\partial\Omega} (\boldsymbol{\tau} \cdot \mathbf{u}) \cdot \mathbf{n} dA - \int_{\partial\Omega} \mathbf{q} \cdot \mathbf{n} dA \quad (2.3)$$

In the equation (2.3) the symbols used to denote the total energy density and the heat flux are  $E$  and  $\mathbf{q}$ , respectively.

The viscous stress tensor  $\boldsymbol{\tau}$  that appears in (2.2) and (2.3) is defined as:

$$\boldsymbol{\tau} = \mu[\nabla \mathbf{u} + (\nabla \mathbf{u})^T] - \frac{2}{3} \mu \nabla \cdot \mathbf{u} \mathbf{I} \quad (2.4)$$

In (2.4), the symbol  $\mu$  represents the dynamic viscosity and  $\mathbf{I}$  stands for the unit tensor.

All the three previous equations follow the same pattern, which can be written in a more general form as:

$$\int_{\Omega} \frac{\partial U}{\partial t} dV + \int_{\partial\Omega} \mathbf{F} \cdot \mathbf{n} dA = 0 \quad (2.5)$$

The symbol  $\mathbf{U}$  stands for the conservative variables vector, while  $\mathbf{F}$  refers to the flux tensor in (2.5). In this case, to be coherent with the three previous equations, the external source strength vector is not taken into account.

In order to get the same equations with this general form, the two new variables introduced in (2.5) are defined as follows:

$$\mathbf{U} = (\rho, \rho\mathbf{u}, \rho E)^T \quad (2.6)$$

$$\mathbf{F} = \mathbf{F}^c - \mathbf{F}^v \quad (2.7)$$

The inviscid flux tensor  $\mathbf{F}^c$ , and the viscous one,  $\mathbf{F}^v$  that appear in (2.7) refer to:

$$\mathbf{F}^c = (\rho\mathbf{u}, \rho\mathbf{u}\mathbf{u} + p\mathbf{I}, (\rho E + p)\mathbf{u})^T \quad (2.8)$$

$$\mathbf{F}^v = (0, \boldsymbol{\tau}, \boldsymbol{\tau} \cdot \mathbf{u} + k(\nabla T))^T \quad (2.9)$$

In (2.9), the symbols  $k$  and  $T$  denote the thermal conductivity and the temperature, respectively.

If the flux tensor is differentiable, by using the Gauss theorem it is possible to write the general equation in a differential form, which is the one used in the discretization of the equations of the problem.

$$\frac{\partial \mathbf{U}}{\partial t} + \nabla \cdot \mathbf{F} = 0 \quad (2.10)$$

The fluid in this case is air. By using the equations of state for perfect gas and the definition of the internal energy,  $e$ , it is possible to deduce the following relationship:

$$p = (\gamma - 1)\rho e = (\gamma - 1)(\rho E - \frac{1}{2}\rho|\mathbf{u}|^2) \quad (2.11)$$

The symbol  $\gamma$  that appears in (2.11) is referring to the ratio of specific heats.

## 2.2. Structure

For similar structures to the one in the case of study, it is possible to follow the classical thin plate mechanics [9] [10]. The Euler-Bernoulli beam model is adopted in order to get the governing equations for the motion of the structure.

Aiming to simplify the problem it is assumed that there is only displacement in the vertical direction, so that the structural problem is one-dimensional. The only external force that is taken into account is the one due to the pressure difference between both upper and lower surfaces of the plate. This 1D simplification is based on the fact that the horizontal displacement of the plate is much smaller than the vertical one. So in first approximation it is possible to neglect it, even though it exists for a real bending beam. The effects of the simplification on the results are expected not to be significant. But it is still necessary to discuss the structure solver results taking this into account.

After these assumptions, the one and only resulting governing equation is the following:

$$M\ddot{w} + C\dot{w} + Bw_{xxxx} = -(p_u - p_l) = -\Delta p \quad (2.12)$$

In (2.12) the vertical displacement is denoted by  $w$ , and the different pressure fields over the upper and lower surfaces of the structure are referred as  $p_u$  and  $p_l$ , respectively.

Regarding the structural properties,  $M$  is the plate's specific mass and it is computed in the following way [10]:

$$M = \rho^s h \quad (2.13)$$

As shown in (2.13), the specific mass of the plate,  $M$ , is equal to the density of the structure,  $\rho^s$  multiplied by its thickness,  $h$ .

The symbol  $B$  denotes the flexural rigidity of the structure. It is related to the Young modulus,  $E^s$ , and the Poisson ratio,  $\nu$ , as follows [10]:

$$B = \frac{E^s h^3}{12(1-\nu^2)} \quad (2.14)$$

In (2.12) the symbol  $C$  is referring to the damping of the structure. In this study the structure is considered to have no damping. So the equation can be simplified and be written in the following form:

$$M\ddot{w} + Bw_{xxxx} = -\Delta p \quad (2.15)$$

This last equation shows how the vertical displacement of the structure is caused by the pressure difference between the two surfaces of the plate, and how it is influenced by its rigidity and mass

### 2.3. Fluid-structure interaction

Once the governing equations for both the fluid and the structure are analyzed in detail separately, it is possible to deal with the whole problem of the interaction between both of them.

Typically both fluid and structure are treated in different ways with regard to the topology of the mesh used.

On the one hand, the fluid is commonly studied in an Eulerian reference frame, where the specifications about its motion are done at certain points [9].

On the other hand, the Lagrangian formulation is the most frequently used when studying the motion of a structure. Unlike the Eulerian formulation, in this case the mesh is stationary. So now the displacements referred to a particular initial configuration are the way of expressing the movement.

Both the Eulerian and the Lagrangian formulations can be combined, but large mesh deformations make structured grids unfeasible. In the case of study the deformations are moderate, so it is possible to use this combination which leads to an arbitrary Lagrangian-Eulerian approach. As a result of this, the mesh now must adapt itself continuously to the boundary of the structure without changing its topology. These modifications have some implications on the flow solver, since it has to obey the geometric conservation law (GCL) for mathematical consistency, in order to solve problems involving flows on moving meshes [11] [12].

This ALE approach also affects the governing equations of the fluid presented in (2.10). Now that the fluid mesh is moving due to the movement of the boundary of the structure, it is necessary to take into account that fluid mesh velocity. So the advection term in the equations should now contain the relative velocity [11].

In terms of modifications to the equations:

The material derivative which normally is presented as:

$$\frac{D}{Dt} = \frac{\partial}{\partial t} + \mathbf{u} \cdot \nabla, \quad (2.16)$$

has to be changed into the following form:

$$\frac{D}{Dt} = \frac{\partial}{\partial t} + (\mathbf{u} - \hat{\mathbf{u}}) \cdot \nabla \quad (2.17)$$

In (2.17) the subtraction of the velocity of the mesh  $\hat{\mathbf{u}}$  to the fluid flow velocity means that the velocity used in the equation is relative to the mesh.

Another aspect to take into consideration is how to achieve the coupling between fluid and solid mechanics [9]. One possibility is to see it as a sequential coupling, where both the fluid and the structure solvers are used one after the other repetitively until the coupling is achieved by iteration. In this case if the fluid solver is used first, the computed pressure difference is passed on to the structure solver and is iterated until convergence is obtained.

But the coupling used in the present method is explicit [6]. In order to achieve this direct coupling, it is necessary to match boundary conditions from both the fluid flow and the structure. The way of proceeding is to match displacement and velocity of the fluid and the structure at the boundary [11].

$$\begin{aligned} y_f &= w \\ \dot{y}_f &= \dot{w} \end{aligned} \quad (2.18)$$

In (2.18),  $y_f$  and  $\dot{y}_f$  denote the displacement and the velocity of the fluid grid points at the interface. By matching them with those from the structure, the problem is coupled and the current solution for the pressure difference from the fluid solver is applicable to the structure solver.

The matching is possible because the grid experiences a boundary fitted re-meshing at every time step. In the fluid domain, the positions and velocities of the points are linearly interpolated using the values from the points of the structure [11].

For the no-slip boundary condition at the interface, the horizontal velocity at the displaced position must be zero. The no-slip condition in the  $y$ -direction is enforced by setting equal both the vertical velocity of the fluid at the interface and the velocity of the structure. Since the velocities are matched, the use of the same time step for both solutions leads to a matching also in accelerations [10].

## 2.4. FSI benchmark

As mentioned before, in order to validate the existing FSI method it is necessary to make a comparison with a FSI experiment. There are some standard FSI test cases such as the ones by Kalmbach and Breuer (2012) [13], Gomes and Lienhart (2010) [14] and Wong (2011) [15]. All of them are useful to make the comparison, but they also have some discrepancies that might be relevant enough to make the validation harder. With regard to the flow regime and the structure configuration, the one presented by Turek and Hron (2006) [16] seems to be the most suitable. So it will be the benchmark for the comparison with the FSI method.

Its main objective is to set a new benchmark which can be used for validations of methods dealing with problems involving fluid-structure interaction [16].

As in the present FSI study, the flow regime is laminar [16]. Nevertheless, the fluid is said to be incompressible, unlike it is in the present case. The compressibility of the fluid is crucial when studying the acoustics of the problem, but in this case it is not relevant for the comparison. So as long as the Mach number is low enough, the results thrown by the method considering the fluid as compressible should not differ from those in the benchmark where the fluid is incompressible. This assumption has to be treated carefully when comparing results.

The configuration of the test case involves an object with flexible parts fully submerged in a channel flow. The FSI leads to self-induced oscillations in the fluid and the structure that affect several physical quantities which are the ones to be compared.

The whole mathematical description of the test case is shown in [16]. The fluid is defined as incompressible and Newtonian, and it is governed by the Navier-Stokes equations just as in the FSI method, but taking into account here that the fluid is incompressible.

Nevertheless, for the structure the difference between FSI method and benchmark model is notable. The structure in the test case is considered to be elastic, as it is in the present FSI model. But the structural model used is different. The structural material is defined by the Cauchy stress tensor, determined by the constitutive law for the St. Venant-Kirchhoff material. So the use of the governing equations for the structure differs from the Euler-Bernoulli beam model used in the present FSI model. Apart from that, it is also remarkable that a simplification is made in the present model considering only a one-dimensional displacement of the structure, whereas the structural model used in [16] is two-dimensional. These differences in

the structural part must be analyzed in detail when making the comparison, to see how the results are affected.

With regard to FSI theory, there are not big differences between what is specified in the benchmark and in the present FSI model. The conditions enforced at the interface imply a balance of forces between fluid and structure and the no-slip condition for the fluid flow.

Once the mathematical description is done in the benchmark, the computational domain is presented, giving all the necessary dimensions and details of the experiment configuration. In Figure 2.2 it is possible to see that the rigid structure is a cylinder. The flexible structure is shown to have a finite thickness, and the whole body is contained in a rectangular channel. Figure 2.3 presents a detailed view of the body to analyze the cylinder junction with the plate and to define the position on the reference points.

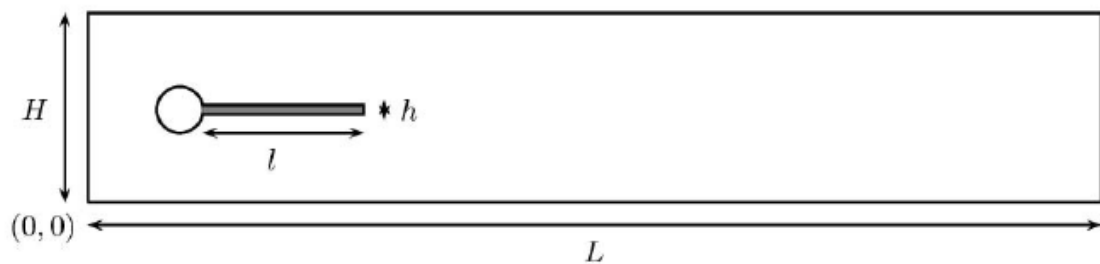


**Figure 2.2.** Test case computational domain (Fig. from [16])

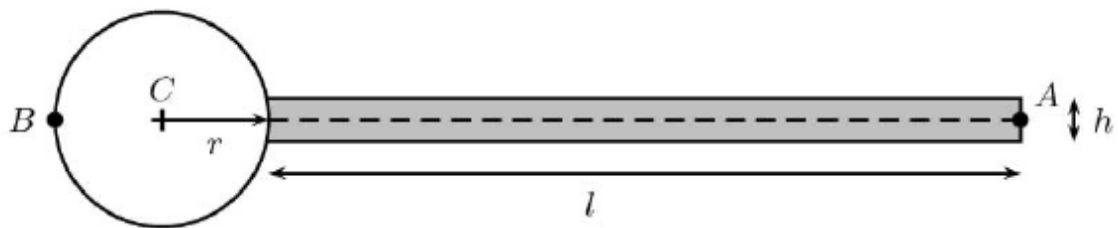


**Figure 2.3.** Detail of the structural part (Fig. from [16])

All the dimensional and positional specifications are summarized in the following table:

**Table 2.1.** Overview of test case geometry parameters (Table from [16])

geometry parameters	value [m]	
channel length	$L$	2.5
channel width	$H$	0.41
cylinder center position	$C$	(0.2, 0.2)
cylinder radius	$r$	0.05
elastic structure length	$l$	0.35
elastic structure thickness	$h$	0.02
reference point (at $t = 0$ )	$A$	(0.6, 0.2)
reference point	$B$	(0.15, 0.2)

Both Figure 2.2 and Figure 2.3, as well as Table 2.1 are directly extracted from [16]. However, the typo of the x-coordinate of reference point B, which was 0.2 m in [16] instead of 0.15 m, is corrected in Table 2.1.

After setting the geometrical configuration of the test case, some specifications about the materials used are made for both the fluid and the structure.

Regarding the fluid, it is relevant to emphasize that the regime must be laminar. This has an implication on the Reynolds number which therefore has to be low enough. Furthermore it is necessary to use a fluid capable of promoting deformations on the structure, so there are some requisites to take into account when choosing the fluid. Therefore, among several possible fluids, the chosen one in [16] is glycerine because of its suitable fluid properties regarding the test case requirements.

At this point it is important to remark that the present FSI model is compatible with gases. There are some equations implemented in the present method such as the equations of state for perfect gas that should be changed in order to simulate the experiment for glycerine. These modifications would mean to re-write parts of the code, which could lead to complications. Nevertheless, the present FSI method solves the problem in a non-dimensional way, the Reynolds number being the essential non-dimensional input parameter. Therefore it is possible to suppose that using the same Reynolds number to simulate the experiment, the flow results should not be different either the fluid is glycerine or a gas.

In other words, although the fluid chosen in the benchmark is glycerine, the present FSI method uses air as the fluid, keeping all the non-dimensional parameters coherent with the air choice (Prandtl number, speed of sound<sup>1</sup> for Mach number, ratio of specific heats etc) but imposing the same Reynolds number as in the benchmark. Both test case and simulation should be equivalent by the equality of the Reynolds number. But this a point to discuss later on when comparing results.

**Table 2.2.** Overview of fluid material parameters (Table from [16])

material	$\rho^f$ [ $\frac{\text{kg}}{\text{m}^3}$ ]	$\nu^f$ [ $10^{-6} \frac{\text{m}^2}{\text{s}}$ ]	$\mu^f$ [ $10^{-3} \frac{\text{kg}}{\text{ms}}$ ]
air	1.23	15	0.018
acetone	790	0.405	0.32
ethyl alcohol	790	1.4	1.1
oil, vegetable	920	76.1	70
water	1000	1.14	1.14
blood	1035	3 – 4	3 – 4
<b>glycerine</b>	1260	1127	1420
honey	1420	7042	10000
mercury	13594	0.0114	1.55

<sup>1</sup> The velocities used in the test case are very small compared to the fluid speed of sound, which leads to very low Mach numbers. Therefore, the CFL condition forces the time step size for Mach number M to be about M times smaller than for incompressible flow. A possible solution would be to artificially increase the Mach number by reducing the speed of sound, so that the problems are avoided and the simulations are speeded up. Obviously the artificial increase of the Mach number is limited in order not to alter the incompressible regime. It is assumed that for a value of the Mach number up to 0.3 the results should not get modified.

For the structure another selection between several materials is done. In this case it is important that the stiffness of the material must be low enough to allow considerable displacements due to the interaction with the fluid. Regarding the specifications, the rubber-like materials such as polybutadiene and polypropylene are suitable.

These materials can be used in the present method when only the structural part is being tested. Nevertheless when the fluid is interacting with the structure, the choice of the structural parameters must be consistent with the choice of the fluid, to get an equivalent situation. So if in the experiment the fluid is glycerine and the solid is polypropylene, the structure in the method has to be such that the interaction with the air is equivalent to the interaction between glycerine and polypropylene.

That means that the ratio between fluid and structure densities must be respected, and the other non-dimensional quantity that has to be conserved from the test case to the FSI method, in order to get the equivalence, is the ratio between the flexural rigidity of the structure and its specific mass.

**Table 2.3.** Overview of solid material parameters (Table from [16])

material	$\rho^s$ [ $\frac{\text{kg}}{\text{m}^3}$ ]	$\nu^s$	$E$ [ $10^6 \frac{\text{kg}}{\text{ms}^2}$ ]	$\mu^s$ [ $10^6 \frac{\text{kg}}{\text{ms}^2}$ ]
<b>polybutadiene</b>	910	0.50	1.6	0.53
polyurethane	1200	0.50	25	8.3
<b>polypropylene</b>	1100	0.42	900	317
PVC	1400	0.42	1500	528
steel	7800	0.29	210000	81400
cork	180	0.25	32	12.8

Both tables presenting the possible choices of materials Table 2.2<sup>2</sup> and 2.3 are extracted straight from [16].

To finish with the mathematical description of the FSI benchmark, it is important to mention some assumptions in the computation of forces such as lift and drag exerted by the fluid on the entire submerged structure. By saying entire structure the purpose is to include both the flexible plate and the rigid cylinder.

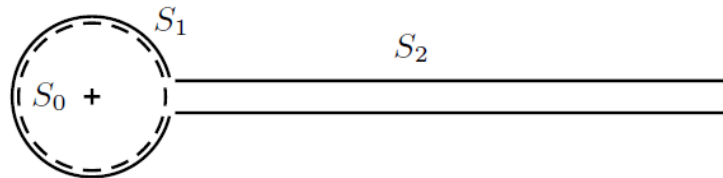


**Figure 2.4.** Integration path for the force calculation (Fig. from [16])

<sup>2</sup> Table 2.2 is directly extracted from [16]. But there is a typo in the value of kinematic viscosity for air. Instead of 0.015 the value in the table should be 15 for air in standard conditions. This correction was done in Table 2.2.

Looking at Figure 2.4 [16] and following the specification of the way of calculating the forces, the integration should be done along the integration path  $S$  which results from the union of two sub-paths:  $S_1$  covers all the surface of the cylinder except for the part in contact with the plate, and  $S_2$  stands for the surface of the plate not taking into account the part fixed to the cylinder. Nevertheless,  $S_0$  makes reference to the whole cylinder surface including the part in touch with the flexible structure.

The assumption made in the benchmark states that the integration along the path  $S$  and the one along the path  $S_0$  both lead to the same results [16]:

$$\int_S \boldsymbol{\sigma} \mathbf{n} dA = \int_{S_0} \boldsymbol{\sigma} \mathbf{n} dA \quad (2.19)$$

This last assumption should be treated carefully by analyzing a specific example: For a uniform pressure on the cylinder and a velocity equal to zero, a pressure difference between the surfaces of the elastic plate is considered. In this case the lift for the cylinder alone would be zero, but taking the plate into account would modify that zero lift. Therefore using the simplification in (2.19) could lead to incorrect results.

Nevertheless, to obtain comparable results, the same assumption is made in the present FSI method. So only the surface of the cylinder,  $S_0$ , is considered as the interface between fluid and structure when computing the forces.

## 2.5. Initial and boundary conditions

To complete the detailed description of the test case, it is necessary to present the initial and boundary conditions that are used for the fluid and the structure.

For the interface between fluid and structure, the no-slip condition is already used in the FSI method. This boundary condition must also be enforced at the channel walls described in the benchmark.

For the fluid flow, there is a boundary condition at the inlet of the channel in order to get a parabolic velocity profile. The parabolic shape of the profile follows the equation given in the benchmark [16]:

$$u^f(0, y) = 1.5\bar{U} \frac{y(H-y)}{\left(\frac{H}{2}\right)^2} \quad (2.20)$$

In (2.20),  $u^f$  stands for the horizontal velocity of the fluid,  $\bar{U}$  refers to the mean inflow velocity and  $H$  denotes the height of the channel. The  $x$ -coordinate of the inlet in (2.20) is set to be zero because the origin of the coordinates system is situated in the lower left corner of the channel. It is remarkable that the maximum inlet velocity occurs exactly in the middle of the channel, while the center of the cylinder is slightly lower. This little difference leads to an asymmetric fluid flow that gives rise to the oscillations of the structure interacting with the fluid. Otherwise, if the maximum velocity were at the same height as the center of the cylinder, the symmetry of the problem would avoid any lift of the structure.

The boundary condition at the outlet of the channel enforces that the gauge pressure must be zero.

$$p'(L, y) = 0 \quad (2.21)$$

The symbols  $p'$  and  $L$  in (2.21) stand for the gauge pressure and the length of the channel, respectively.

Regarding the initial conditions for the fluid flow, the initial horizontal velocity is set to be zero in the whole fluid domain except for the inlet, where the  $x$ -component of the velocity profile is determined by the boundary condition (2.20). The  $y$ -component of the velocity is initially zero everywhere. Initial pressure and density are set to their stagnation values.

Moreover, it is recommended in the benchmark to use a starting procedure (for unsteady test cases) in order to get a smooth increase in time of the velocity profile at the inlet [16].

$$u^f(t, 0, y) = \begin{cases} u^f(0, y) \frac{1 - \cos(\frac{\pi t}{2})}{2}, & \text{if } t < 2 \\ u^f(0, y), & \text{otherwise} \end{cases} \quad (2.22)$$

(2.22) shows that the velocity profile at the inlet starts from zero at  $t=0$  and ends with the parabolic velocity profile described in (2.20) at  $t=2$ .

For the structure there are two boundary conditions. For the leading edge of the flexible plate, the boundary condition sets a clamped configuration (the leading edge of the structure is fixed to the cylinder), so both the vertical displacement and the velocity of the structure are equal to zero at this point [10].

$$\begin{aligned} w_1 &= 0 \\ \frac{\partial w}{\partial x} \Big|_1 &= 0 \end{aligned} \quad (2.23)$$

The variable  $w_1$  that appears in (2.23) refers to the vertical displacement of the leading edge of the flexible plate at the height of the center of the cylinder. The index 1 denotes the grid point  $x_1$ .

For the trailing edge of the structure the boundary condition corresponds to a free configuration, being the shear force and the bending moment equal to zero [10]:

$$\begin{aligned} \frac{\partial^2 w}{\partial x^2} \Big|_N &= 0 \\ \frac{\partial^3 w}{\partial x^3} \Big|_N &= 0 \end{aligned} \quad (2.24)$$

In (2.24) the index  $N$  refers to the last grid point of the flexible structure, which is situated at the trailing edge.

The initial condition for the structure is already imposed by the geometry parameters of the benchmark presented in Table 2.1. The trailing edge of the flexible plate is called reference point A, and it is specified that the height of reference point A at time equal zero is the same as the height of the center of the cylinder. Since the leading edge of the plate is fixed to the cylinder at the height of its center, this means that at the initial time the position of the structure is horizontal, or in other words, there is not initial displacement for the flexible structure.

$$w_i(t = 0) = 0 \quad , i = 1, \dots, N. \quad (2.25)$$

The subscript  $i$  in (2.25) denotes the index of grid point  $x_i$ .

Once the governing equations and the boundary and initial conditions for the whole problem are defined, its mathematical description is completed, and it is ready to be discretized.

## 2.6. Non-dimensional perturbation form

As it was mentioned before, the FSI method solves the equations in a non-dimensional form. The independence on dimensions makes it easier to carry out a specific simulation. For example in this case, there is only need to change a couple of non-dimensional parameters for the fluid and the structure and the whole test case can be simulated.

In the following, it is shown how the main flow and structural variables are made non-dimensional.

For the fluid motion, the chosen reference values are stagnation values:  $\rho_0$  for the density,  $c_0$  for the speed of sound and  $L$  as the characteristic length scale of the domain.

In this case both reference values for density and speed of sound correspond to the fluid used in the FSI method. As it was discussed above, the fluid is assumed to be air instead of glycerine, so the reference values are the ones from air to be consistent with the assumption.

For the characteristic length scale of the domain one should look at the definition of the Reynolds number done in the benchmark [16].

$$Re = \frac{d\bar{U}}{\nu^f} \quad (2.26)$$

The parameters used in the definition of the Reynolds number are the diameter of the cylinder  $d$ , the mean inflow velocity  $\bar{U}$  and the kinematic viscosity of the fluid  $\nu^f$ . The Reynolds number has to be the same in the FSI method in order to mimic the experiment. So the characteristic length scale of the domain is set to be equal to the diameter of the cylinder.

So using the three reference values for density, velocity and length it is possible to do the non-dimensionalization of all the physical quantities involved in the problem. By developing the transformation of the flow equations with the choices of reference values, it is deduced that the continuity, momentum and energy equations, as well as the equations of state, have the exact same form in both dimensional and non-dimensional formulations. This means that the

flow equations do not need to be changed, it is just necessary to use the non-dimensional quantities with the same equations.

Moreover the present FSI method solves the problem in a perturbation formulation. The conservation laws of mass, momentum and energy are expressed in terms of the changes of the conservative variables, the stagnation values being the references. The same perturbation formulation is extended to the equations of state as well.

As an example of this formulation, it is easy to see the definition for the density:

$$\rho = \rho_0 + \rho' \quad (2.27)$$

$$\rho' = \rho - \rho_0$$

In (2.27) the index 0 denotes the reference value and the apostrophe refers to the perturbation form. Therefore the definition of the perturbation quantity is the difference between the real value and the reference one. The same formulation is done for the rest of the conservative variables in order to get the same governing equations but in a non-dimensional perturbation form.

As for the flow equations, the structure governing equations must be expressed in a non-dimensional formulation as well. The choice for the reference quantities remains on the structural part, being the stagnation density, speed of sound and the characteristic length scale of the domain the ones used to make non-dimensional the rest of the physical quantities.

Going through the formulation of the equations it results to be, as it was in the fluid part, that the transformed governing equation for the structure has exactly the same form in both dimensional and non-dimensional formulations. Therefore, there is no need to change the equation. But the specific mass, flexural rigidity and pressure difference must be used in their non-dimensional form to get the results non-dimensional as well.

### 3. Numerical models

Once all the details of the mathematical description of the whole problem are determined, the process must continue by getting everything prepared for the numerical computations. In order to do so, it is necessary to describe the space and time discretizations used in the FSI method for both the fluid and the structure solver.

In this section all the numerical aspects related to the FSI method are treated, and some explanations about the numerical models for fluid and structure are given. Then the implementation of the fluid-structure interaction is studied by analyzing its algorithm.

Several modifications on the computational domain need to be done in order to simulate the experiment using the FSI method. There are also some changes necessary related to the block

structure. After going through all the numerical parts of the problem, by the end of this section the FSI method will be fully outlined.

### 3.1. Fluid

The computational model of the fluid flow solver works with the equations in a non-dimensional perturbation formulation. The reason for the perturbation form comes from the fact that the difference between the values of a physical variable, e.g. pressure, in one grid point and its neighbors might get almost imperceptible. By using the perturbation formulation instead of the pressure values, only the pressure perturbations are used, being able to avoid cancellation errors in the values of the pressure difference between neighbor grid points.

For the discretization of the governing equations used in the fluid solver, a coordinate transformation needs to be done. The coordinates  $x$  and  $y$  from a physical domain are transformed into a computational domain where the coordinates are  $\xi$  and  $\eta$ . The time  $t$  is also transformed into  $\tau$ .

In order to do so, the new coordinates  $\xi$  and  $\eta$  are defined as functions of the old coordinates and time  $(x,y,t)$ . The new time  $\tau$  is set to be equal to the old time  $t$ . The transformation of coordinates is fully developed and the time derivative of the Jacobian determinant is given by the geometric conservation law [6] [12]:

$$(J^{-1})_{\tau} + (J^{-1}\xi_t)_{\xi} + (J^{-1}\eta_t)_{\eta} = 0 \quad (3.1)$$

Then the Jacobian determinant of the transformation  $J$ , is integrated in time using the classical fourth order explicit Runge Kutta method. Once the discretization of the equations is done, the domain has to be discretized as well. At this point it is useful to remind what the FSI method is originally made for, by looking at the original computational domain for the case in the upper airways. From that domain and with the same logic, the new computational domain for the case of the benchmark has to be created.

Figure 3.1 [11] shows the multi-block structured grid representing the simplified geometry in the upper airways.

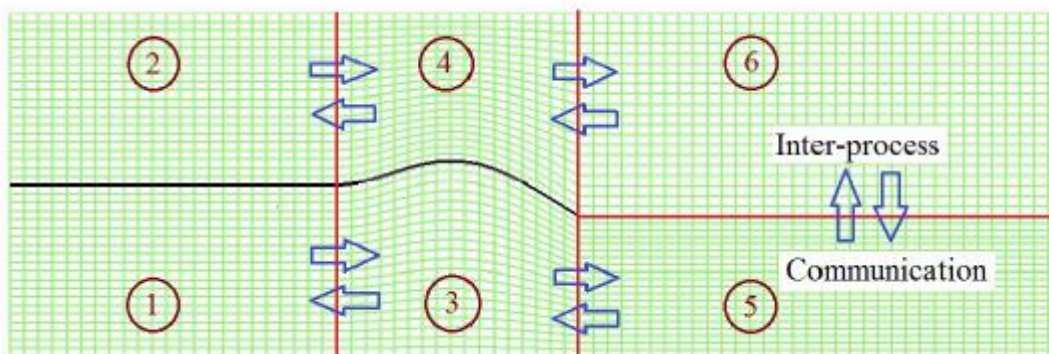


**Figure 3.1.** Original computational domain for the case in the upper airways (Fig. from [11])

The first thing that needs to be modified is the shape of the fixed structure, which in the FSI experiment is a cylinder instead of a plate. This change has implications both on the topology of the grid surrounding the fixed structure and on the block structure. Regarding the mesh surrounding the cylinder, now the grid lines have to be able to adapt themselves to the shape of the cylinder, being similar to those surrounding the flexible plate but independent of time since the cylinder is not moving. With the new configuration there is a need of two more blocks right before the cylinder, in order to get the upstream fluid flow, making a total of eight blocks.



**Figure 3.2.** Schematic of the block structure for the FSI experiment

By comparing both Figure 3.1 and Figure 3.2 some differences are clear. The increase in the total amount of blocks from six to eight, and the change in the shape of the structure were already mentioned. But they also cause some changes in the inter-block communication. That is due to the increase in the number of blocks, which leads to a new communication system involving the new blocks. But the mechanism of inter-block communication is unchanged. In both figures the red lines represent the boundaries between blocks where the communication is allowed and the arrows stand for the double direction of each inter-block communication.

The inter-block communication is achieved by using the message passing interface, such that each block is assigned to a single processor, enabling a parallel solution of the fluid flow field. Therefore some ghost points are indispensable for the sending and receiving information between neighbor blocks at the boundaries where the inter-block communication is allowed.

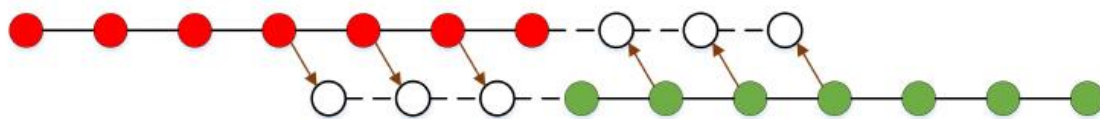


**Figure 3.3.** Schematic of points overlapping along a line (Fig. from [11])

In Figure 3.3 [11], the red and green dots are internal points in the left and right blocks, respectively. The white dots are ghost points overlapping the internal points in the other blocks. The arrows indicate the direction of data transfer between the blocks. At a block boundary, the seven-point stencil of the sixth order central finite difference method needs three ghost points on either side.

By implementing in the present FSI method all the commented changes involving the shape of the fixed structure, the multi-block structure and keeping the MPI communication mechanism in the specified inter-block boundaries, the new computational domain valid for the benchmark case is obtained, cf. Figure 3.4.

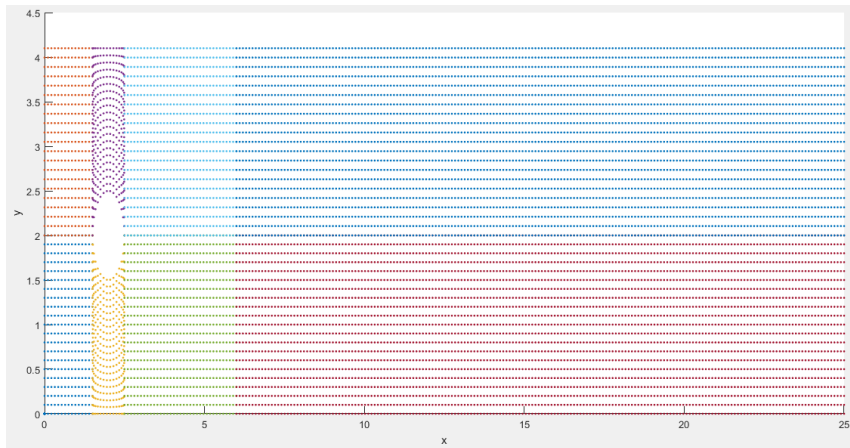


**Figure 3.4.** Computational domain for the simulations

In Figure 3.4 it is possible to see the new distribution of the eight blocks contained in the computational domain, as the different colors of the grid points represent different blocks. The grid lines in blocks surrounding the cylinder are now adapted to its shape. For doing so, with a given number of grid points the grid spacing along the cylinder surface is chosen to be constant, while in the vertical direction an interpolation is needed to get the appropriate shape. The length scales of the domain have been made non-dimensional by using the diameter of the cylinder as the characteristic length scale. Analyzing the figure carefully it is possible to see that the center of the cylinder is not exactly in the middle of the channel but at height 2.0, a fact that avoids symmetry and gives rise to the oscillating motion of the flexible structure interacting with the fluid. It is also possible to see how the elastic structure is treated as a thin plate with no thickness, unlike it is in the benchmark.

The grid size is 253 x 41, i.e. 253 and 41 grid points in the x- and y-directions, respectively. In the blocks that are not containing the cylinder, the grid spacing is equidistant in both directions. The number of grid points, the grid spacing and the angle of grid lines, they all have direct implications on the results. So they will be analyzed in detail in section 4 when treating the obtained results.

The fluid computational model is based on a sixth order finite difference discretization in space, where it is important to remark the use of summation by parts (SBP) operators. These finite difference operators aim to mimic integration by parts, being the use of SBP operators a mathematical tool to ensure the stability and accuracy of the high order scheme. Physically this is describing that the final energy must be lower than the initial one, so that the whole process is stable in terms of energy.

As indicated before in Figure 3.3, for the standard sixth order central finite difference method the stencil is containing seven points. In case a boundary between two different blocks is allowed to communicate, the communication requires an overlap of three points at both sides of the boundary in order to achieve the inter-block communication which enables a parallel solution for the fluid flow field.

For the discretization in time, the method used is the classical fourth order explicit Runge-Kutta method. Furthermore at the end of each time step the use of a sixth order explicit filter helps suppressing possible undamped modes.

The scheme used in the FSI method presents two conditions that must be respected in order to avoid numerical problems related to the stability of the scheme [17].

$$\frac{(|u| + c)\Delta t}{\Delta x} + \frac{(|v| + c)\Delta t}{\Delta y} \leq 2 \quad (3.2)$$

$$\frac{\nu\Delta t}{\Delta x^2} + \frac{\nu\Delta t}{\Delta y^2} \leq 1.5$$

In the general stability conditions shown in (3.2) the symbol  $u$  refers to  $x$ -velocity component,  $v$  to  $y$ -velocity component,  $c$  to speed of sound and  $\Delta t$ ,  $\Delta x$  and  $\Delta y$  to time step size and grid spacings, respectively. The symbol  $\nu$  denotes the kinematic viscosity multiplied by a factor as shown in (3.3) [17], where  $\mu$  is the dynamic viscosity,  $\rho$  the density,  $\gamma$  the ratio of specific heats and  $Pr$  denotes the Prandtl number.

$$\nu = \frac{\mu}{\rho} \max\left\{\frac{4}{3}, \frac{\gamma}{Pr}\right\} \quad (3.3)$$

### 3.2. Structure

As in the fluid part, the numerical model for the structure works with the governing equation in a non-dimensional formulation. With regard to the space discretization of the structure it is considered as infinitely thin, unlike in the benchmark where it has a finite thickness.

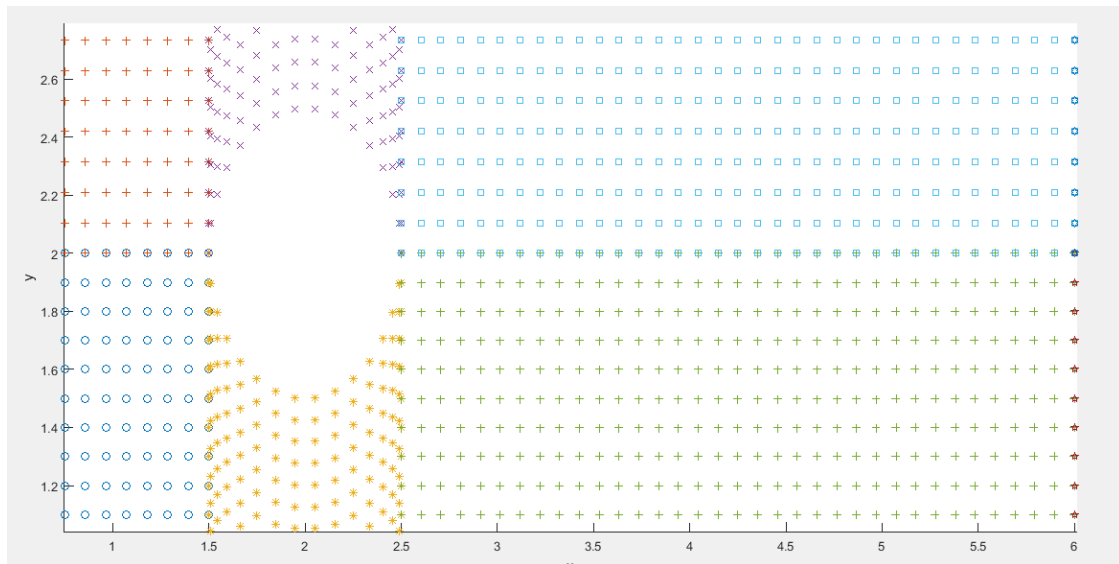


**Figure 3.5.** Detail of the structure in the computational domain

It is shown in Figure 3.5 that just a grid line at height  $y=2.0$  is representing the whole flexible structure, containing the grid points at the interface which are also considered as part of both

the upper and lower blocks of the fluid domain. The whole structure including the cylinder and the plate is considered as a wall so that that the communication through it is not allowed. That is shown in Figure 3.2 where it is possible to observe how the structure avoids the inter-block communication between blocks 3-4 by the cylinder and blocks 5-6 by the plate.

Moreover it is important to remind that a simplification was made for the displacement of the structure, assuming that the only possible movement of the plate is vertical, which leads to a simplified one-dimensional problem.

In terms of space discretization of the governing equation, a central finite difference scheme is used for the space derivative in (2.12).

$$w_{xxxx}|_i = \frac{1}{\Delta x^4} (w_{i+2} - 4w_{i+1} + 6w_i - 4w_{i-1} + w_{i-2}) \quad (3.4)$$

Regarding the boundary conditions for the flexible structure at the leading and trailing edges presented in (2.23) and (2.24), respectively, the space discretization using the finite difference method enables to deduce the following relationships between the closest grid points to the leading and trailing edges:

$$\left. \frac{\partial w}{\partial x} \right|_1 = \frac{w_2 - w_1}{\Delta x} = 0; \quad w_2 = w_1 = 0 \quad (3.5)$$

By using the forward finite difference method at the leading edge in (3.5), the relationship between the vertical displacements of the two first grid points of the flexible structure is known. The third grid point of the structure starting from the leading edge uses these two values from (3.5) to be able to compute (3.4). Also for the last grid point of the structure it is necessary to develop the boundary conditions at the trailing edge from (2.24).

$$\left. \frac{\partial^2 w}{\partial x^2} \right|_N = \frac{w_{N+1} - 2w_N + w_{N-1}}{\Delta x^2} = 0; \quad w_{N+1} = 2w_N - w_{N-1} \quad (3.6)$$

$$\left. \frac{\partial^3 w}{\partial x^3} \right|_N = \frac{w_{N+2} - 3w_{N+1} + 3w_N - w_{N-1}}{\Delta x^3} = 0; \quad w_{N+2} = 3w_N - 2w_{N-1}$$

Once the relationships between the displacements of the two last grid points of the structure are known, it is possible to compute the displacement at the trailing edge using (3.4), completing the space discretization of the governing equation for all grid points belonging to the structure.

For the time discretization of the governing equation, it is necessary to solve the transient dynamics of the structure. The Newmark time integration method is used in order to get the dynamic system modelled, achieving stability and second order accuracy by the use of this scheme [18].

The time derivative terms in the governing equation for the structure (2.12) are discretized using the Newmark method's parameters:

$$\dot{w}_{t+\Delta t} = \dot{w}_t + \Delta t((1 - \gamma)\ddot{w}_t + \gamma\ddot{w}_{t+\Delta t}) \quad (3.7)$$

$$w_{t+\Delta t} = w_t + \dot{w}_t \Delta t + \Delta t^2 \left( \left( \frac{1}{2} - \beta \right) \ddot{w}_t + \beta \ddot{w}_{t+\Delta t} \right) \quad (3.8)$$

In both equations (3.7) and (3.8) it is possible to see how the parameters  $\gamma$  and  $\beta$  from the Newmark method play a role, leading their choice to a wide range of different solutions. Therefore the value of these two parameters must be carefully chosen.

$$\beta = \frac{1}{4} \quad (3.9)$$

$$\gamma = \frac{1}{2}$$

The value of the parameter  $\beta$  shown in (3.9) is commonly used, since it yields to a constant average acceleration method. The choice of  $\gamma$  in (3.9) is simply in order to avoid numerical damping which can appear with a different value of this parameter [19].

### 3.3. Fluid-structure interaction

The computational models for the fluid and the structure are already presented, but since this whole project work is about the interaction between both of them, it is clear that the numerical model of the problem must include a detailed explanation of how the fluid-structure interaction is implemented in the existing method.

The FSI algorithm has to be analyzed carefully, and some explanations of the internal part of the method are necessary to be able to understand how it works and uses a multi-block communication to achieve a parallel solution.

For a general problem involving FSI, the algorithm must start by giving the initial values for both the fluid and the structure, so that the initial mesh for the fluid can be generated based on the initial configuration of the structure. Once the entire initial configuration of the problem is well defined, the process for the first time step will be repeated at every time level until the final time is reached.

This mentioned process starts with the computation at the interface of the stress coming from the fluid flow, which enables to calculate the pressure difference  $\Delta p$  at the flexible plate at that specific time level. At this point the fluid solver advances one step in time to get a preliminary state of the fluid flow for the next time level. Then the structure solver starts to work taking the  $\Delta p$  information from the old time level in order to compute the displacement of the structure for the new time level.

Now that the displacement of the structure is known, the fluid mesh and the velocities of its grid points must be recalculated based on the solution given by the structure solver. Once the fluid grid is updated, the same process is repeated from that time level on until the final time step [6].

For an easier comprehension of the FSI algorithm described above it is useful to see it in a schematic way. The Figure 3.6 taken from [11] makes it possible.

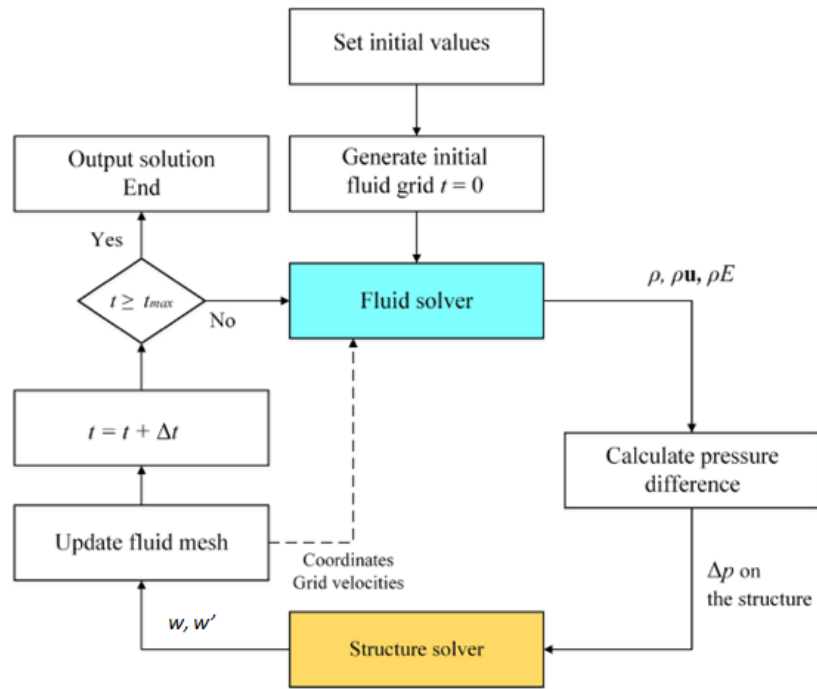


**Figure 3.6.** Schematic of the FSI algorithm of the method (Fig. from [11])

After getting a general idea of how the FSI is implemented in the method, its numerical code must be analyzed in order to fully understand the whole mechanism of the program, and to be able to know where to make modifications if necessary for the development of the project work.

The method is written in a very extensive FORTRAN code structured as a main program and calls for a big list of subroutines, each of them aiming to a particular purpose. Among all the subroutines, some of them are dedicated to enabling the MPI for the inter-block communication and the parallel solution, while others establish all the necessary parameters to get the correct domain. There are also subroutines thought to ensure the stability of the scheme and the list goes on until the last detail of the method is covered.

Just after a detailed analysis of the code it is possible to make the necessary modifications to simulate the FSI experiment using the existing method. The block structure, the computational domain, the fluid mesh and the initial and boundary conditions among others, must be changed in order to get the existing method ready for the simulation and start getting results for the comparison with the FSI benchmark.

## 4. Results

After presenting the theoretical background of the fluid-structure interaction problem and its numerical solution by a detailed mathematical description and the definition of the numerical models, the whole simulation process is ready to be started. The numerical results obtained

from the FSI method in this section have to be compared with those given as a reference in the FSI experiment. For doing such a comparison the simulation process must be conducted following carefully all the guidelines specified in the benchmark.

The reference results from the FSI experiment are obtained for a fully developed flow during one entire period of oscillation. Some of the quantities that must be computed for comparison are the displacement of the trailing edge of the structure or the lift and drag forces on the whole surface of the structure due to the interaction with the fluid.

When giving time dependent results, the line of action is to specify mean value, amplitude and frequency calculated for one whole period of oscillation. Also for the time dependency a plot of the results is required to analyze their development in time.

In the benchmark all the tests are performed using several different levels of refinement and after this grid-refinement study, an almost grid-independence of the given reference results is remarked. A similar study is carried out regarding the time step size, using several of them for each test case to analyze what effects they have on the results.

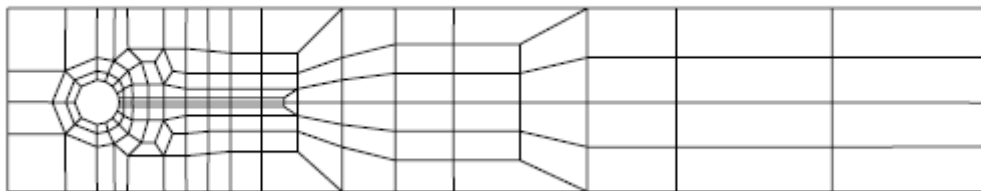


**Figure 4.1.** Example of a coarse mesh from the FSI benchmark (Fig. from [16])

**Table 4.1.** Grid refinement levels from the FSI benchmark (Table from [16])

level	#refine	#el	#dof
0+0	0	62	1338
1+0	1	248	5032
2+0	2	992	19488
3+0	3	3968	76672
4+0	4	15872	304128

Both Figure 4.1 and Table 4.1 are directly extracted from [16]. At this point it is important to say that the mesh type shown in Figure 4.1 differs from the one used in the FSI method presented in Figure 3.4. Unlike the structured grid of the present method, the mesh from the FSI benchmark shows an irregular pattern for the cells surrounding the whole structure, which enables to accumulate a large number of grid points close to the body for a higher accuracy of the results. The grid shown in Figure 3.4 might present some problems of convergence due to the big jumps in cell sizes and angles presented at both sides of the cylinder. This fact has to be taken into account when presenting the results of the fluid solver.

In the benchmark the test cases of study are divided into three different parts. The reason for that organization is to carry out the validation of both the fluid and structure solvers

separately first, to finish with the validation of the whole FSI method afterwards. Therefore, the structural test cases, called CSM tests in the benchmark, are presented first. Right after, the fluid solver is checked for the CFD tests. Finally the FSI tests consider the cases where the interaction between fluid and structure is studied.

#### 4.1. CSM Tests

The purpose of these tests is to validate the structure solver used in the present FSI method. In order to do so, the flexible part of the structure must be isolated forgetting about the surrounding fluid. This enables to test the structural solver alone and avoids fluid-structure interaction computations that are unnecessary for this specific case.

The motion, which is caused by the pressure difference in the normal FSI case, is now due to the gravitational force that must be included in the governing equation for the structure.

$$M\ddot{w} + Bw_{xxxx} = -Mg \quad (4.1)$$

The governing equation for the CSM tests (4.1) is the same as the governing equation for the structure presented in the mathematical description (2.15) with the only difference of the external force, which is changed from the pressure difference between upper and lower surfaces of the plate to the gravitational force. The symbol  $g$  in (4.1) denotes the absolute value of the gravitational acceleration in the vertical direction, and the new term on the right hand side of the equation represents the gravity force per unit area which now is counted at every grid point of the flexible structure.

Three different partial tests are defined in the benchmark for the structural part: Test CSM3 simulates a time dependent case starting from the initial configuration of the flexible plate. The two other tests CSM1 and CSM2 are steady state solutions<sup>3</sup>.

The dimensional and non-dimensional structural parameters needed for the simulation of each case are given in the benchmark [16].

**Table 4.2.** Overview of parameters for structural tests (Table from [16])

par.	CSM1	CSM2	CSM3
$\varrho^s \left[ 10^3 \frac{\text{kg}}{\text{m}^3} \right]$	1	1	1
$g \left[ \frac{\text{m}}{\text{s}^2} \right]$	2	2	2
$\nu^s$	0.4	0.4	0.4
$E^s \left[ \frac{\text{kg}}{\text{ms}^2} \right]$	$1.4 \times 10^6$	$5.6 \times 10^6$	$1.4 \times 10^6$

It is not specified in [16] but the absolute value of the gravitational acceleration used in the tests is clearly artificial, not corresponding to the real value of this acceleration on earth.

---

<sup>3</sup> The present method computes the time dependent solution while tests CSM1 and CSM2 represent the steady state solutions. For the comparison in those cases, the steady state solution will be approximated by the mean value of the time dependent solution from the present method.

Looking at (4.1) it is possible to see that the input parameters that the method needs for the simulation are the specific mass and the flexural rigidity of the flexible structure. By using the relationships presented in (2.13) and (2.14) with the value for the thickness of the plate specified in Table 2.1, the necessary parameters M and B can be calculated for each of the structural test cases. They are presented in Table 4.3.

**Table 4.3.** Input parameters for structural tests

Par.	CSM1	CSM2	CSM3
$M \left[ \frac{\text{kg}}{\text{m}^2} \right]$	20	20	20
$B \left[ \frac{\text{kg} \cdot \text{m}^2}{\text{s}^2} \right]$	1.11	4.44	1.11

As explained in the section of the non-dimensional formulation, the governing equation for the structure in the CSM tests has the same form either it is used in a dimensional or non-dimensional way. In this case, since the structure is isolated, the dimensional input parameters are used, so the results will be dimensional as well and fully comparable with those given as reference.

For the grid refinement study the simulations are done for three different levels of refinement like in the benchmark. The present results either correspond to the coarse, medium or fine grid, the number of grid points along the structure being 51, 101 and 201 respectively.

The different time steps used in the simulations are exactly the same as in the benchmark ( $\Delta t$  equal to 0.02 s, 0.01 s and 0.005 s), so that the time step influence is comparable.

The first test case to be analyzed is CSM3, to do the time development study first, and then the two steady cases follow.

#### 4.1.1. CSM3

In order to have a general idea of how the structure moves, the following two figures show the displacement of the whole flexible structure for the coarse grid using a time step equal to 0.02 seconds.

The displacement shown in Figure 4.2 corresponds to the time increment between  $t=0$  s and  $t=2$  s.

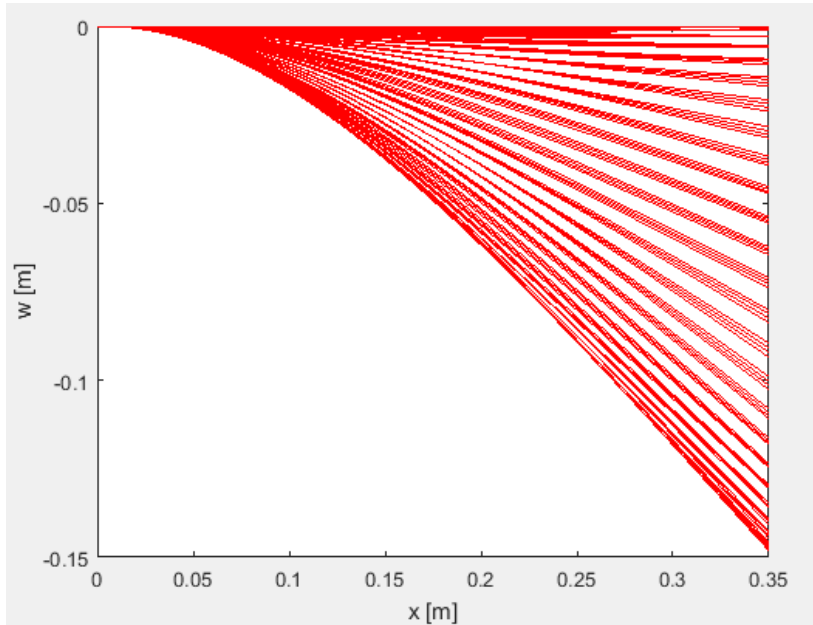


**Figure 4.2.** CSM3 Displacement of the whole structure (every 2 seconds)

In Figure 4.2 it is possible to observe the oscillating movement of the whole flexible plate caused by the gravitational force that was added specifically for the CSM tests.

To be able to see the displacement development in time in more detail, Figure 4.3 shows only the first oscillation of the whole simulation, since it is then when the maximum displacement (0.148136 m) takes place.

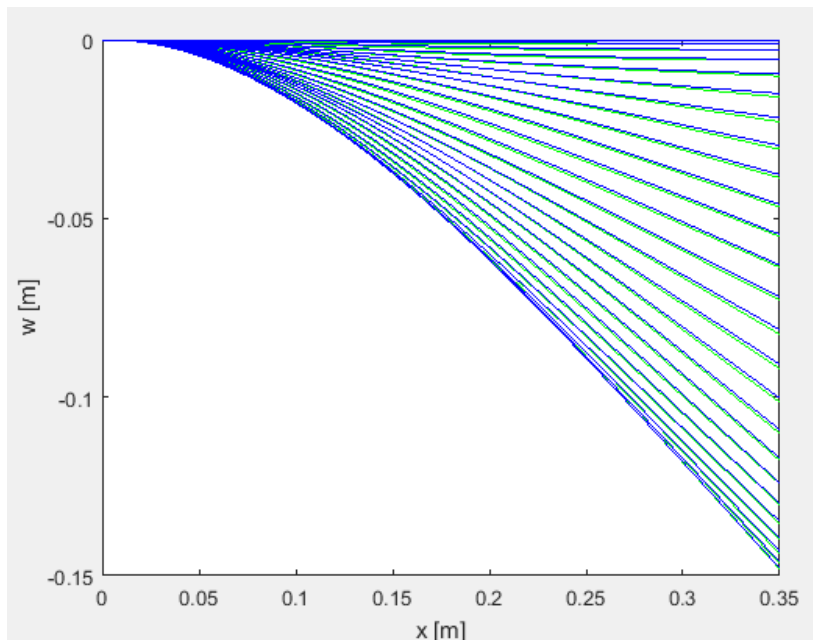


**Figure 4.3.** CSM3 Displacement of the whole structure: First oscillation (1 second)

In Figure 4.3, the time increment of the displacement shown is 1 second. The downward and upward displacements of the plate are represented by the green and blue lines, respectively.

The results that are given as reference in the benchmark are both the horizontal and vertical displacements of the trailing edge of the structure, or as defined in Table 2.1, the reference point A. Nevertheless it is important to remark that the 1D simplification assumed for the Euler-Bernoulli beam model yields only one governing equation for the vertical direction, so the only displacement computed by the present structure solver is the vertical one. Therefore, all the comparisons between the results and the reference values are made only for the vertical displacement  $w$ .

The plots in Figures 4.4-4.12 represent the development in time of the computed vertical displacement of the trailing edge for ten seconds. The red dots refer to the results of the present structure solver, and the blue line denotes the reference values given in the benchmark [16].

All the results for the three different time steps using each of the three levels of grid refinement studied are presented together below, in order to easily compare them and be able to discuss the grid refinement and time step studies.

- $\Delta t = 0.02$  s

Coarse: 51 grid points

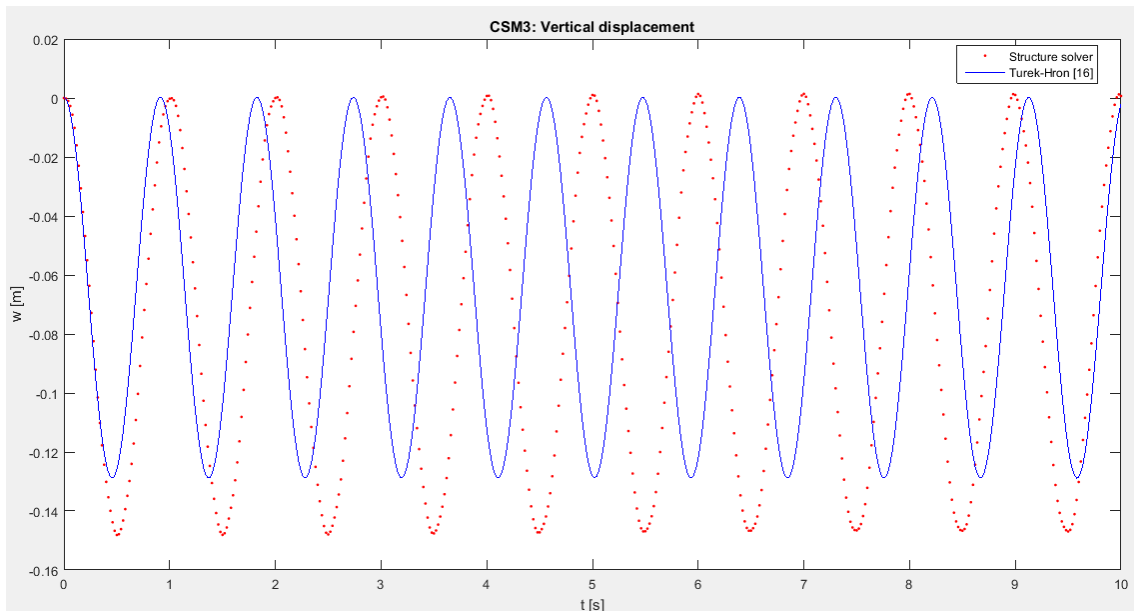


**Figure 4.4.** CSM3:  $\Delta t = 0.02$  s. Coarse grid

Medium: 101 grid points

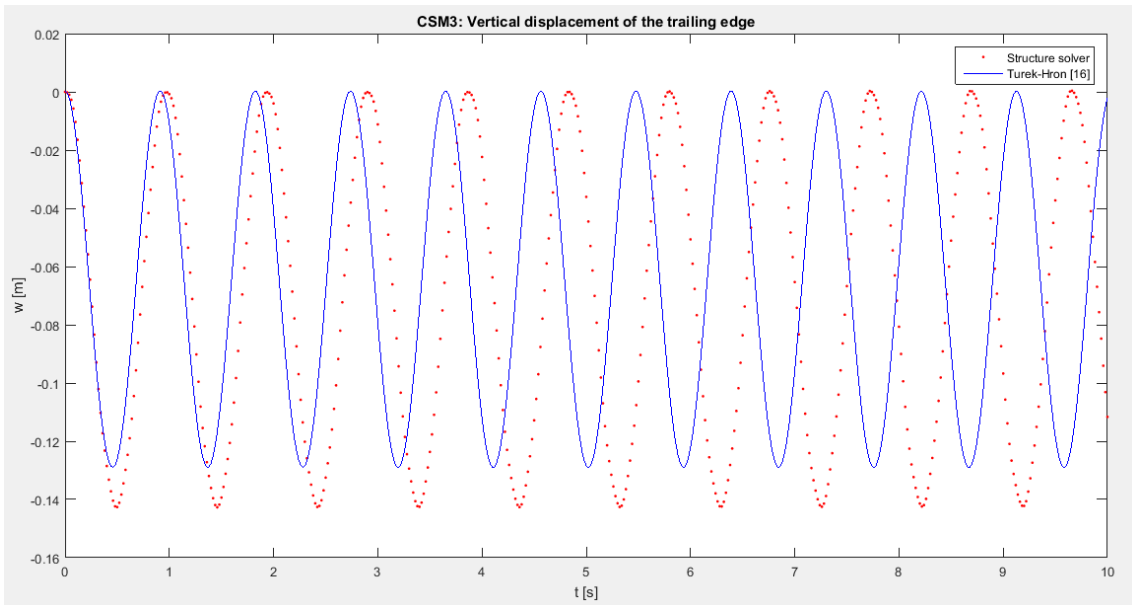


**Figure 4.5.** CSM3:  $\Delta t = 0.02$  s. Medium grid

Fine: 201 grid points

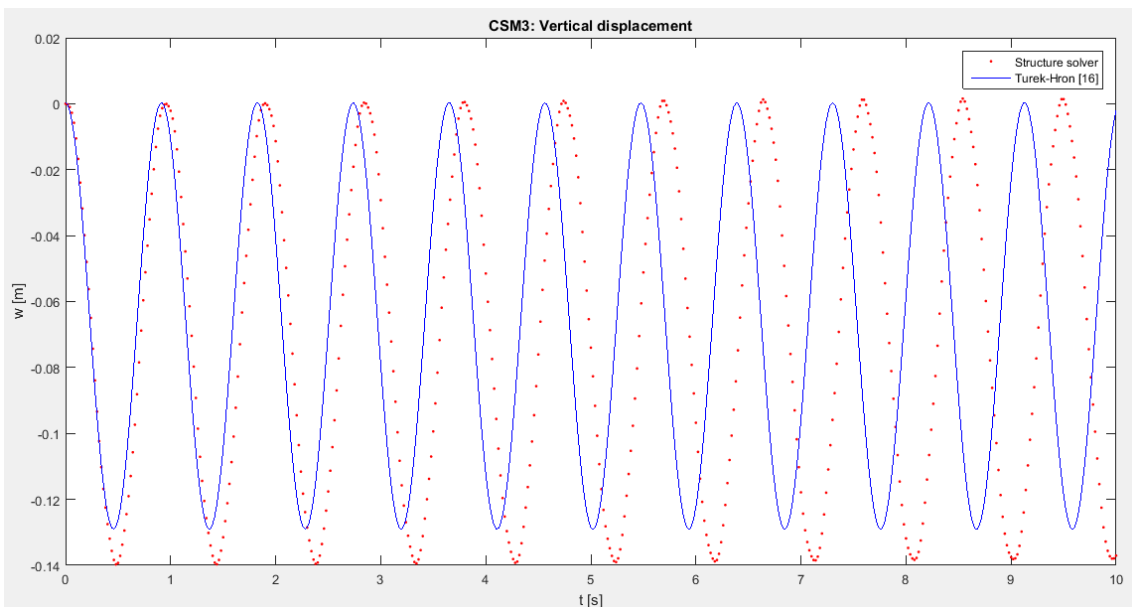


**Figure 4.6.** CSM3:  $\Delta t = 0.02$  s. Fine grid

- $\Delta t=0.01$  s

Coarse: 51 grid points

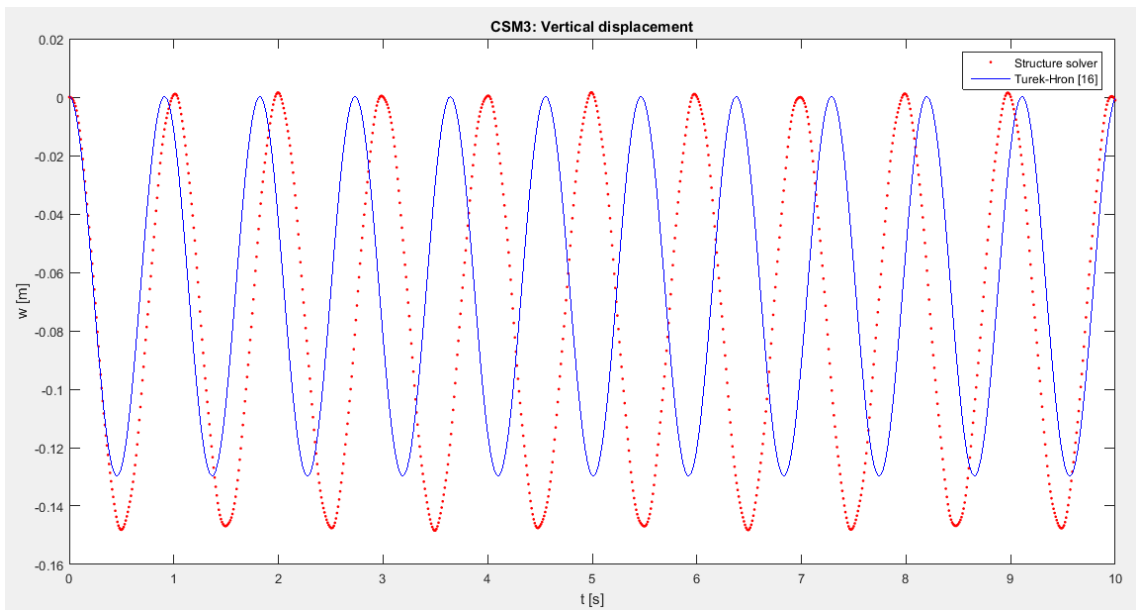


Figure 4.7. CSM3:  $\Delta t = 0.01$  s. Coarse grid

Medium: 101 grid points

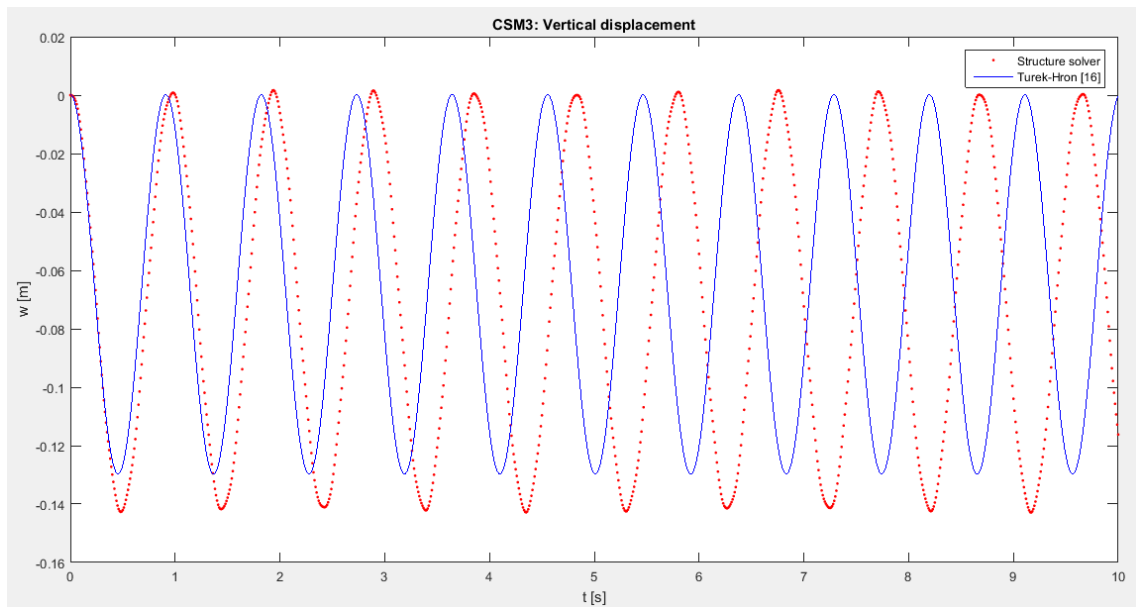


Figure 4.8. CSM3:  $\Delta t = 0.01$  s. Medium grid

Fine: 201 grid points

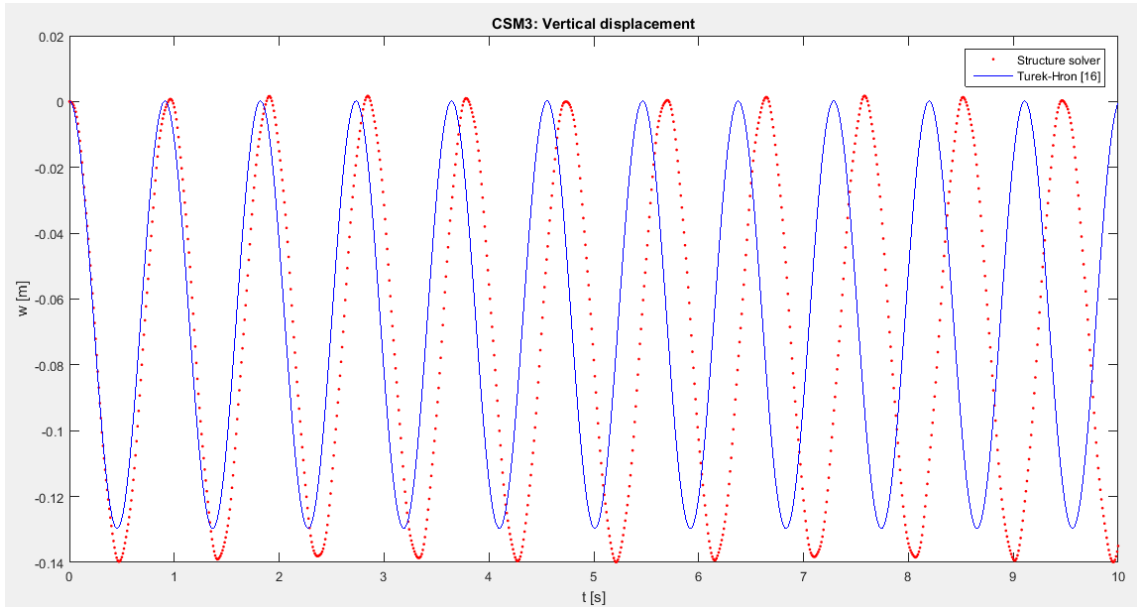


Figure 4.9. CSM3:  $\Delta t = 0.01$  s. Fine grid

- $\Delta t = 0.005$  s

Coarse: 51 grid points

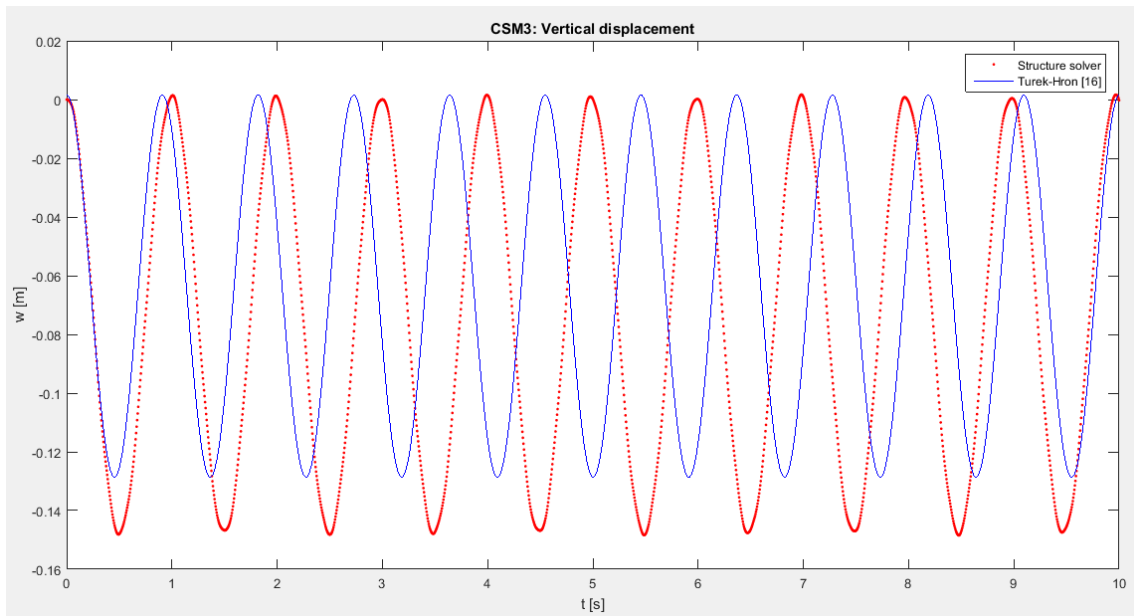
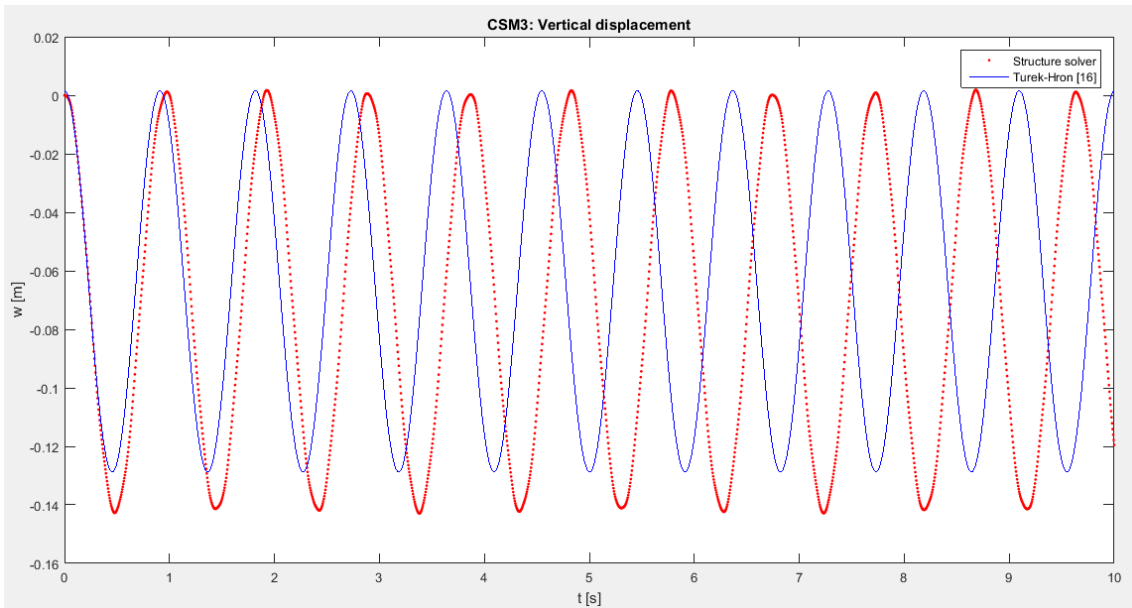


Figure 4.10. CSM3:  $\Delta t = 0.005$  s. Coarse grid

Medium: 101 grid points



**Figure 4.11.** CSM3:  $\Delta t = 0.005$  s. Medium grid

Fine: 201 grid points

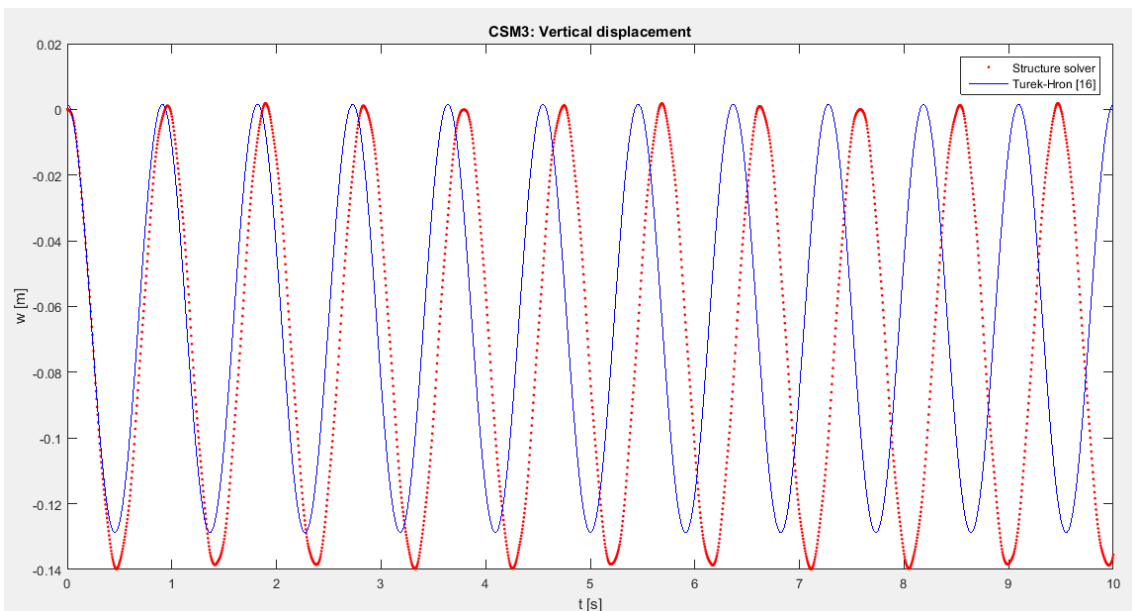


**Figure 4.12.** CSM3:  $\Delta t = 0.005$  s. Fine grid

The numerical results corresponding to all the plots presented in Figures 4.4-4.12 above are arranged and summarized in Table 4.4. As commented at the beginning of the results section, the time dependent results must be given specifying the mean value, the amplitude and the frequency (appears between brackets in the tables of time dependent results). The mean value is determined as the average of the maximum and minimum values of the last period of the oscillations. The difference between those two values is divided by two in order to compute the amplitude. Finally the frequency is determined as the inverse of the period, which is computed as the difference between the end and start time values of the last period of the oscillations.

**Table 4.4.** CSM3 results: Time step and grid refinement studies

<b>CSM3: Vertical displacement of the trailing edge [10E-3 m]</b>			
	<b>Grid refinement</b>	<b>Turek-Hron [16]</b>	<b>Structure solver</b>
<b><math>\Delta t = 0.02</math> s</b>	Coarse	-64.271 ± 64.595[1.0956]	-72.949 ± 73.970[1.0000]
	Medium	-64.352 ± 64.679[1.0956]	-71.306 ± 71.263[1.0204]
	Fine	-64.371 ± 64.695[1.0956]	-69.093 ± 69.929[1.0638]
<b><math>\Delta t = 0.01</math> s</b>	Coarse	-64.744 ± 64.907[1.0978]	-72.639 ± 74.265[1.0204]
	Medium	-64.765 ± 64.946[1.0978]	-71.252 ± 71.246[1.0417]
	Fine	-64.766 ± 64.948[1.0978]	-69.989 ± 69.954[1.0582]
<b><math>\Delta t = 0.005</math> s</b>	Coarse	-63.541 ± 65.094[1.0995]	-73.686 ± 74.671[0.9804]
	Medium	-63.594 ± 65.154[1.0995]	-69.747 ± 71.342[1.0526]
	Fine	-63.607 ± 65.160[1.0995]	-68.608 ± 69.793[1.0695]
	<b>Reference</b>	<b>-63.607 ± 65.160[1.0995]</b>	

In Table 4.4 all the numerical results of the structure solver are presented, including the three levels of refinement for each of the three different time steps. The numerical results of the benchmark are given as well. It is important to remark that the present grid sizes and the ones used by Turek and Hron cannot be compared directly, since only the total number of elements and degrees of freedom are given in [16].

It is deduced from Figures 4.4–4.12 and Table 4.4 that the results obtained by the present structure solver show larger (in absolute value) mean values and amplitudes of the oscillations than the results extracted from the benchmark. With regard to the frequencies of the oscillations, they are smaller than in the benchmark results, or in other words, the periods of oscillations are larger for the present structure solver results.

In order to find an explanation of these results it is convenient to remind the 1D simplification made for the equations of the present structure solver. For simplifying the structure movement to a vertical displacement there are some implications on the results. When a real beam is bending each of its points is suffering both a vertical and a horizontal displacement, and this movement in the horizontal dimension is being neglected in the method due to the 1D simplification. Therefore if this horizontal displacement is not taken into account, as in the present structure solver results, the absolute value of the vertical displacement gets increased

and so do its mean value and amplitude. The effect is the same for the period which is bigger for those increased displacements, what means that the frequencies are smaller.

To carefully analyze the size of the errors in the structure solver results it is useful to look at the first oscillations of the plots. In Figure 4.13 it is possible to see in detail the first two seconds of simulation of the case shown in Figure 4.12, in which the smallest time step and the finest grid are used.

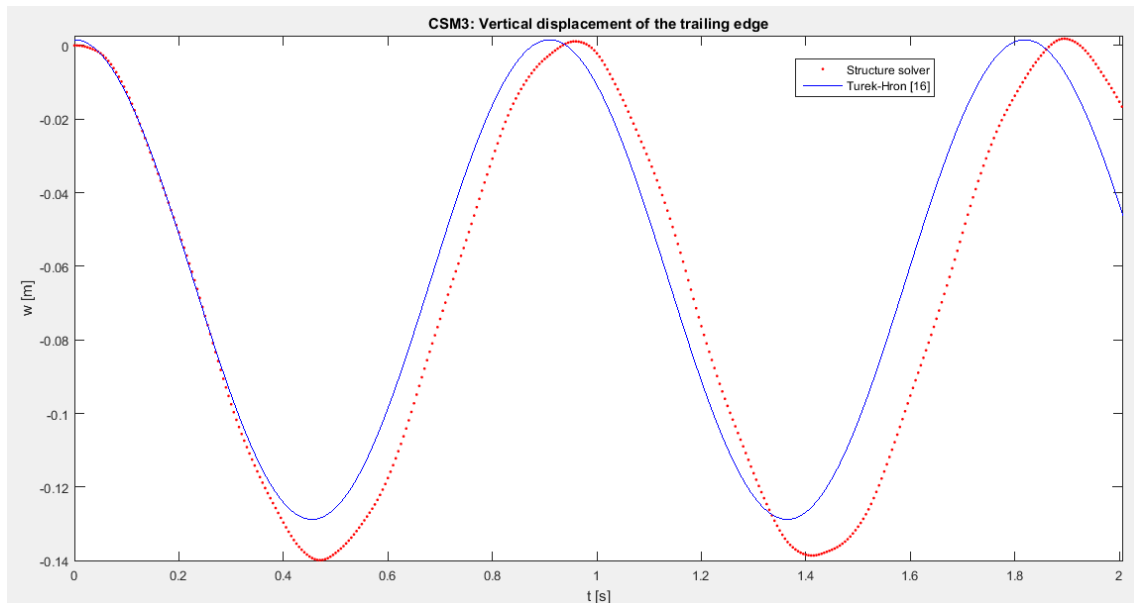


**Figure 4.13.** First oscillations of CSM3:  $\Delta t = 0.005$  s. Fine grid

The real differences between the results from the structure solver and the benchmark can be observed by analyzing the first oscillation. It is shown there how the trailing edge is moving with larger absolute values of mean value and amplitude, which lead to longer periods of oscillations according to the numerical results. When time goes on, the slightly bigger period appears for each of the oscillations and therefore, for longer times the plot of the structure results gets delayed with respect to the reference results plot as shown in Figures 4.4-4.12.

Regarding the grid refinement study in Table 4.4, the structure solver results show a tendency of getting closer to the reference values when the number of grid points increases. In other words, the finer the grid gets, the higher the accuracy of the results is. Once this obvious effect of the grid refinement is confirmed, it is possible to compare both refinement studies from the structure solver and the benchmark. The influence of the refinement level is shown to be much bigger in the structure solver results than in the reference results where, as it is claimed in the benchmark, the results are almost grid independent.

The reason for that bigger grid refinement dependence of the structure solver results is the low number of grid points used. Even though three refinements are done, the highest number of grid points is probably not as high as it is in the benchmark. That means that if starting from the current finest grid, three more grid refinements are done (401, 801 and 1601 number of grid points, respectively), then the structure solver results will show less dependence on the number of grid points. Keeping on this methodology, the results at the end are expected to tend to grid refinement independence, but this is something to be shown.

The time step study evidences similarities between the present structure solver results and those from the benchmark. It is possible to see in Table 4.4 how the size of the time step used affects the results obtained. Starting from the largest time step and reducing it repetitively leads to small variations of the results. The given reference value corresponds to the one obtained using the smallest time step size.

Since the CSM3 test case is not describing a steady state but a stable state for oscillating solutions, this dependence on the time step is expected. When the level of refinement is already high enough, as it is in the benchmark, a change in the size of the time step has a bigger influence on the results than a grid refinement.

Aiming to evaluate the accuracy of the structure solver, the relative errors of the displacements must be computed after the comparison of the structure solver results with the ones given as a reference in the benchmark.

**Table 4.5.** CSM3: Relative error of the results

<b>CSM3: Vertical displacement of the trailing edge. Relative errors (%)</b>				
	<b>Grid refinement</b>	<b>Mean value</b>	<b>Amplitude</b>	<b>Frequency</b>
<b><math>\Delta t = 0.02</math> s</b>	Fine	8,62	7,32	-3,25
<b><math>\Delta t = 0.01</math> s</b>	Fine	10,03	7,36	-6,24
<b><math>\Delta t = 0.005</math> s</b>	Fine	7,86	7,11	-2,73

In Table 4.5 the relative errors for the mean value, amplitude and frequency of the oscillating displacement are presented. Even though in the benchmark there are also three levels of refinement, they are probably not completely equivalent to the refinement levels used in the present structure solver. This means that the considered coarse grid in the benchmark might suit better with the medium level of the present structure solver instead of with the coarse one. Therefore, the computation of the relative errors is made only for the finest grid of the present structure solver for each of the time step sizes. To determine the relative errors in Table 4.5, the “exact result” used is the one given as a reference in Table 4.4 corresponding to the use of the finest grid and the smallest size of the time step.

The obtained relative errors are commented at the end of the structural results section together with the errors from the test cases CSM1 and CSM2.

After this time development study carried out for the test case CSM3, the two other time independent test cases are analyzed.

#### **4.1.2. CSM1**

As shown in Table 4.3 this test case and CSM3 consider the exact same parameters for the mass and rigidity of the structure. Nevertheless, CSM1 presents the steady state solution. For the present structure solver results, the steady state solution will be approximated by the mean value of the time dependent solution in CSM3, in order to make the comparison possible.

As in the previous test case, the results are shown first and the discussion and computation of relative errors follow.

**Table 4.6.** CSM1 results: Grid refinement study

<b>CSM1: Vertical displacement of the trailing edge [10E-3 m]</b>		
<b>Grid refinement</b>	<b>Turek-Hron [16]</b>	<b>Structure solver</b>
Coarse	-66.0263	-73.6858
Medium	-66.0817	-69.7472
Fine	-66.0965	-68.6083
<b>Reference</b>	<b>-66.10</b>	

The structure solver results shown in Table 4.6 represent the mean value of the displacement for the time dependent solution using the smallest time step  $\Delta t=0.005$  s. It is possible to see how the obtained results are larger in absolute value than those in the benchmark [16]. The value given as reference in [16] corresponds to the steady state solution obtained using the finest grid.

As it was explained in the CSM3 discussion of results, these differences are due to the 1D simplification made for the structure solver governing equations. The lack of displacement in the horizontal direction leads to larger vertical displacements.

The grid refinement study shows the big dependence on the number of grid points of the structure solver results, compared to the ones from the benchmark. The low number of grid points used in the present solver, for the three levels of refinement, impedes to get grid independence that was achieved in the benchmark. It could only be reachable by continuing the grid refinement study for even finer grids.

For a better understanding of the results and to get an idea of the comparison, it is relevant to compute the relative error of the results.

**Table 4.7.** CSM1: Relative error of the results

<b>CSM1: Vertical displacement of the trailing edge</b>	
<b>Grid refinement</b>	<b>Relative error (%)</b>
Fine	3,80

Table 4.7 gives the relative error of the structure solver result for the finest grid compared to the reference one shown in Table 4.6. As explained before for the CSM3 test case, it only makes sense to compute it for the finest grid level, because the levels of refinement defined in the structure solver and in the benchmark might not be equivalent one by one.

### 4.1.3. CSM2

This is the last test case studied for the structural part of the problem and the process is exactly the same as in test case CSM1. As in the previous test case, the steady state solution is given. So in order to make a comparison, the steady state solution will be approximated by the mean values of the oscillating solution obtained using the present structure solver.

Regarding the structural parameters used in this test case, there is a remarkable difference with respect to CSM1 and CSM3. According to Table 4.3, the flexural rigidity chosen for this case is four times the one used in the other two test cases, while the specific mass of the plate is unchanged in relation to them. Therefore, smaller displacements of the structure are expected, but in order to confirm this supposition it is necessary to analyze the results in Table 4.8 obtained for the smallest time step  $\Delta t=0.005$  s.

**Table 4.8.** CSM2 results: Grid refinement study

<b>CSM2: Vertical displacement of the trailing edge [10E-3 m]</b>		
<b>Grid refinement</b>	<b>Turek-Hron [16]</b>	<b>Structure solver</b>
Coarse	-16.9536	-18.3659
Medium	-16.9684	-17.4813
Fine	-16.9723	-17.1803
<b>Reference</b>	<b>-16.97</b>	

As expected, the results in Table 4.8 show much smaller displacements (in absolute value) of the trailing edge of the flexible plate than those in Table 4.6. The increase in the rigidity of the plate for the same mass implies that a bigger force is needed to have the same displacement. Since the gravitational force is the same in both cases, according to Table 4.2, the flexible plate experiences smaller vertical displacements. The reference result given in [16] is the one corresponding to the finest grid.

Analyzing both the structure solver and the benchmark results [16] in Table 4.8, the 1D simplification assumed for the present structure solver is the cause for larger vertical displacements as in the two previous test cases.

In relation to the grid refinement study made in Table 4.8, the results for the three different levels of refinement present smaller differences among them than in the other two cases of study. Nevertheless, the relative differences are similar to the ones in the previous test cases. It is clear anyway that these differences are still much bigger than the ones in the benchmark, which present almost grid independence due to a higher number of grid points along the structure.

For a quantitative comparison of the results, the relative errors are computed in Table 4.9.

**Table 4.9.** CSM2: Relative error of the results

<b>CSM2: Vertical displacement of the trailing edge</b>	
<b>Grid refinement</b>	<b>Relative error (%)</b>
Fine	1,23

Again the only level of refinement taken into account to compute the relative error in Table 4.9 is the finest one, as in test cases CSM1 and CSM3. To determine this relative error, the reference value shown in Table 4.8 is used.

Once all the three structural test cases of study are completed it is time for a global overview of the results obtained in this section.

In order to qualify the accuracy of the results thrown by the structure solver, the relative errors in Table 4.5, Table 4.7 and Table 4.9 must be analyzed.

For the time dependent test case CSM3, the relative errors are approximately 7% for the mean value and the amplitude of the vertical displacement of the trailing edge, while the frequency shows a 3% relative error. When considering the mean value of the stable time dependent solution for the vertical displacement in test cases CSM1 and CSM2, the accuracy of the structure solver looks to be slightly higher showing a reduction in the obtained relative errors. The error goes down to a 4% in CSM1 and to an even lower 1% in the case CSM2, where the rigidity of the flexible plate has been increased.

Therefore and according to all the results obtained and discussed in this section, it is reasonable to assume that the accuracy of the structure solver is high enough. So the results obtained by using it may be considered as valid.

## **4.2. CFD Tests**

In this section the fluid flow is analyzed not taking into account its interaction with the flexible structure. In order to isolate the fluid flow, it is suggested in the benchmark to consider the flexible plate as a rigid object by setting very high values for its density and shear modulus, or either defining the fluid domain with only fixed boundary conditions along the interface with the plate. But the easiest way to do it with the existing method is to “disconnect” the structure solver, so that the pressure difference is computed but not used to calculate the displacement of the plate. Therefore, the structure just acts as a fixed submerged body in the fluid flow.

Three different subtests called CFD1, CFD2 and CFD3 are proposed for this fluid solver validation. The setting up of the parameters for all of them is given in [16] and summarized in Table 4.10.

**Table 4.10.** Parameter setting for the CFD tests (Table from [16])

dimensional parameter	CFD1	CFD2	CFD3
$\rho^f [10^3 \frac{\text{kg}}{\text{m}^3}]$	1	1	1
$\nu^f [10^{-3} \frac{\text{m}^2}{\text{s}}]$	1	1	1
$\bar{U} [\frac{\text{m}}{\text{s}}]$	0.2	1	2
non-dimensional parameter	CFD1	CFD2	CFD3
$\text{Re} = \frac{Ud}{\nu^f}$	20	100	200

At this point, it is important to remind the assumptions made for the fluid at the mathematical description section for simulating the FSI experiment. First of all, the fluid under consideration is a gas (air in particular) to avoid possible numerical problems in the existing method, which is made for gases. Nevertheless, the fluid defined by the properties in Table 4.10 is glycerine, which is an incompressible fluid. It is assumed that the difference on the fluid choice should lead to equivalent results if the Reynolds number is the same in both cases.

Therefore, the only parameter that must be strictly respected is the Reynolds number. This non-dimensional parameter is directly given as an input parameter of the FSI method. The characteristic velocity used in the FSI method is the speed of sound, so the non-dimensional mean inflow velocity coincides with the definition of the Mach number, and through this non-dimensional parameter is how it enters the method.

The Mach number for all the test cases in this section is set to be 0.2, even though the inlet velocities and the speed of sound lead to much lower values. If the real values were used, the acoustic waves would be reflected several times for a small advance of the flow, which could lead to numerical issues and long simulations. The solution based on setting a larger Mach number (by an artificial decrease of the speed of sound) should not affect the results, if the chosen Mach number respects the incompressible flow regime, i.e. Mach number lower than 0.3 approximately. Also within this incompressible regime, the fact that the method uses the compressible Navier-Stokes equations should not be relevant for the obtained results.

Due to the different methods of integration in time used in the fluid solver and in the benchmark, it might not be possible to use the same time steps for all the simulation cases. The non-dimensional parameter representing the time step in the existing method must be chosen to respect the stability conditions of the scheme, coming from the viscous terms of the equations and from the computation of the Courant number as shown in (3.2).

The last aspect to clarify before getting started with the simulations is that the results obtained using the method are non-dimensional, while the ones given as reference are not. Therefore, it is necessary to express one of them into the other's form. Since the quantities for comparison are the lift and drag forces, the easiest way to do this is to compute the lift and drag coefficients of the reference results as shown in (4.2), and then compare them to the results from the FSI method.

$$C_L = \frac{L}{\frac{1}{2} \rho \bar{U}^2 d \cdot 1m} \quad (4.2)$$

$$C_D = \frac{D}{\frac{1}{2} \rho \bar{U}^2 d \cdot 1m}$$

The symbols that appear in (4.2) are L and D standing for lift and drag forces respectively,  $\bar{U}$  referring to the mean inflow velocity for each test case, and  $\rho$  and  $d$  denoting the density of the fluid and the diameter of the cylinder. As a 2D problem the width of the cylinder is considered to be equal to one meter.

First the steady state cases CFD1 and CFD2 are considered, before turning to the time dependent case CFD3 at the end of the section.

#### 4.2.1. CFD1

According to Table 4.10 the Reynolds number is set to be 20 for this simulation. As the fluid used is supposed to be air, the Prandtl number and the ratio of specific heats are unchanged from the original problem in the upper airways, with values of 1 and 1.4 respectively. A Mach number of 0.2 is used following the assumption explained before.

The grid used for the simulation of the test case is shown in Figure 3.4, and in relation to it, the non-dimensional time step utilized is  $\Delta t=0.002$ , respecting the CFL condition and the stability condition derived from the viscous terms of the Navier-Stokes equations in (3.2). The duration of the simulation has to be long enough to ensure that the steady state solution is achieved.

The reference results presented in the benchmark are given in Table 4.11 which is directly extracted from [16]. An extensive grid refinement study, with ten different levels of refinement, is done to show the almost grid independence of the results in [16].

**Table 4.11.** CFD1: Reference results (Table from [16])

level	nel	ndof	drag	lift
0 + 0	144	3032	$1.41635 \times 10^{+01}$	$1.15592 \times 10^{+00}$
1 + 0	576	11536	$1.42236 \times 10^{+01}$	$1.11747 \times 10^{+00}$
2 + 0	2304	44960	$1.42730 \times 10^{+01}$	$1.11692 \times 10^{+00}$
3 + 0	9216	177472	$1.42880 \times 10^{+01}$	$1.11852 \times 10^{+00}$
4 + 0	36864	705152	$1.42919 \times 10^{+01}$	$1.11896 \times 10^{+00}$
5 + 0	147456	2811136	$1.42927 \times 10^{+01}$	$1.11904 \times 10^{+00}$
5 + 1	150528	2869504	$1.42929 \times 10^{+01}$	$1.11906 \times 10^{+00}$
5 + 2	156672	2986240	$1.42929 \times 10^{+01}$	$1.11905 \times 10^{+00}$
5 + 3	168960	3219712	$1.42929 \times 10^{+01}$	$1.11905 \times 10^{+00}$
6 + 0	589824	11225600	$1.42929 \times 10^{+01}$	$1.11905 \times 10^{+00}$
ref.			14.29	1.119

In order to do the comparison, the reference values from Table 4.11 have to be expressed in non-dimensional form by the use of (4.2).

**Table 4.12.** CFD1: Non-dimensional reference results

	Drag and lift coefficients	
	CD	CL
Reference	7,145	0,560

Once the reference values for comparison are established, the first results of the present fluid solver are obtained. These results are not comparable to the reference values, since they indicate problems with the fluid grid that are impeding the solution from reaching the steady state. Moreover, at some points of the simulation the computed drag coefficients are negative, which contradicts the basic principles of fluid mechanics. It is obvious that the negative drag results are wrong, since even zero drag in d'Alembert's paradox is contradictory.

In order to analyze the convergence of the solution, it is useful to compute the change in time of the conservative variables as shown in (4.3).

$$\Delta U_{i,j}^n = U_{i,j}^{n+1} - U_{i,j}^n \quad (4.3)$$

The symbol U in (4.3) represents a conservative variable in general, showing that the increment is computed in the same way for all of them ( $\rho$ ,  $\rho u$ ,  $\rho v$  and  $\rho E$ ). These changes are used to calculate the Euclidean norm of the residual (summing the changes squared of all the conservative variables) in (4.4).

$$\|\Delta res^n\|_{Eu} = \sqrt{\sum_{i,j} ((\Delta \rho_{i,j}^n)^2 + (\Delta \rho u_{i,j}^n)^2 + (\Delta \rho v_{i,j}^n)^2 + (\Delta \rho E_{i,j}^n)^2)} \quad (4.4)$$

Once the Euclidean norm is computed for each time step of the simulation, its development in time can be plotted to see the tendency of the residual.

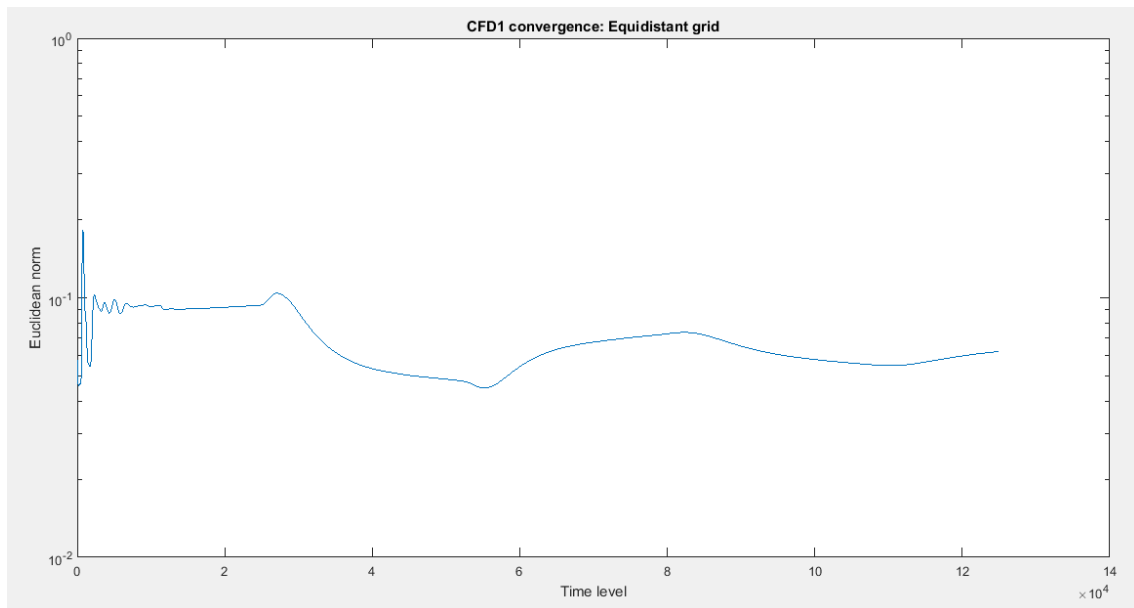


**Figure 4.14.** CFD1: Convergence of the solution. Equidistant grid

From Figure 4.14 it is possible to see how the Euclidean norm of the residual barely changes from the beginning of the simulation and does not tend to a lower value, as it should if the steady state solution was reached. By analyzing in more detail each of the increments of the conservative variables, it seems that the one which varies the most is  $\Delta pE$ . Therefore, it is interesting to plot the value of this quantity at the last time step for the whole domain.

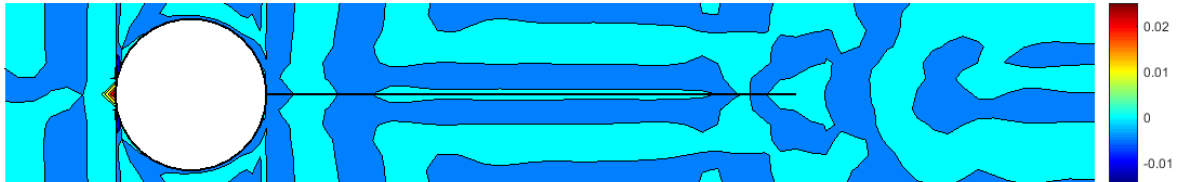


**Figure 4.15.** Detail of the values for  $\Delta pE$  surrounding the structure

By looking carefully at Figure 4.15, one can see that at the leading edge of the cylinder (defined as reference point B in Figure 2.3) the largest value for  $\Delta pE$  occurs. It is coherent to assume that the convergence stagnates at that exact point with a value of  $\Delta pE = 0.0289$ , while the change of this conservation variable is practically equal to zero in the rest of the domain.

The problem probably comes from the creation of the grid at the leading and trailing edges of the cylinder, where the big jumps in the cell sizes and angles lead to poor metric terms  $x_{\eta}$  and  $y_{\eta}$ . As a consequence of that, the flow results and the computed lift and drag forces are affected. The leading edge, where the pressure is largest, seems to be more critical than the trailing edge.

At this point, two possibilities are considered to alleviate the problems caused by the grid at both the leading and the trailing edges of the cylinder. On the one hand, a modification on the inter-block communication mechanism at the problematic zones would solve the issues caused by the jumps in the cell sizes. However, a rearrangement of the grid points in those zones could be done, helping in the same way as the first possibility. The solution based on modifying the communication mechanism involves some changes to the current inter-block communication algorithm, which would require rewriting parts of the original code of the FSI method. To avoid that, the solution adopted is the one consisting in a grid modification.

Due to the constant arc length between neighbor grid points along the cylinder, the sizes of the cells in x-direction get smaller when approaching the leading or trailing edges. Nevertheless, for the rest of the blocks the grid is equidistant so the size of the cells is constant, which leads to big jumps of the cell sizes on both sides of the cylinder. Therefore, it is necessary to decrease the size of the cells that are close to the cylinder, which can be done by using some clustering functions to accumulate grid points near the cylinder. Moreover, a clustering also in y-direction can be useful to get more grid points contained in the boundary layer, which is crucial to get accurate results when the Reynolds number gets larger.

The same clustering mechanism is used for both directions, and considering  $N$  grid points the two different functions that are used were proposed by Roberts (1971) [20]. One leads to a clustering towards the first grid point (4.5) and the other one towards the last grid point (4.6).

$$x_i = x_1 + (x_N - x_1) \left( 1 + \beta \frac{1 - \left(\frac{\beta + 1}{\beta - 1}\right)^{1 - \frac{i-1}{N-1}}}{1 + \left(\frac{\beta + 1}{\beta - 1}\right)^{1 - \frac{i-1}{N-1}}} \right), i = 1, \dots, N. \quad (4.5)$$

$$x_i = x_N - (x_N - x_1) \left( 1 + \beta \frac{1 - \left(\frac{\beta + 1}{\beta - 1}\right)^{1 - \frac{N-i}{N-1}}}{1 + \left(\frac{\beta + 1}{\beta - 1}\right)^{1 - \frac{N-i}{N-1}}} \right), i = 1, \dots, N. \quad (4.6)$$

The subscript  $i$  in (4.5) and (4.6) denotes the index of the grid points, and  $\beta$  is a parameter which must be strictly greater than 1.

For the clustering in the  $x$ -direction, the parameter  $\beta$  is selected aiming to match the cell size on both sides of the block boundaries situated at the leading and trailing edges. In the case of the  $y$ -direction clustering, the criterion for choosing  $\beta$  is to accumulate a certain number of grid points within the boundary layer, but since its thickness is not known along the cylinder, it ends to be a matter of trial and error.

After implementing the mentioned modifications in the fluid mesh of the existing method, the obtained computational domain is shown in Figure 4.16. Considering the three vertical inter-block boundaries (for the whole height of the channel) from left to right, the values of the  $\beta$  parameter are 1.0185, 1.0223 and 1.346. The value of  $\beta$  used for the clustering in the  $y$ -direction is 1.1.

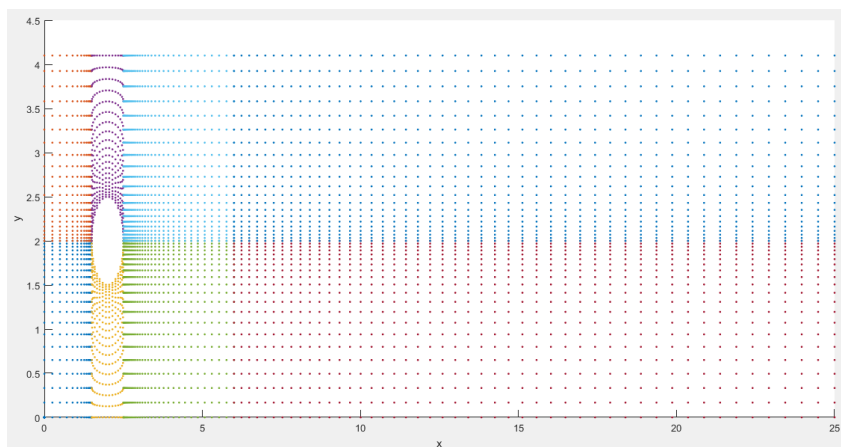


**Figure 4.16.** Computational domain using grid clustering

It is possible to observe the influence of the clustering in the grid by looking at Figure 4.16, where an accumulation of grid points is taking place at the surroundings of the cylinder and at the middle of the channel. The  $\beta$  choice for the rightmost vertical inter-block boundary has

some implications. The first grid spacing of the last column of blocks is smaller than the one needed to match the clustering. Therefore, a reduction in the number of grid points of the last two blocks is needed. The implications on the results should not be relevant, since the flow at the end of the channel does not require such a big amount of grid points.

So the number of grid points along the x-direction of the two blocks behind the flexible structure decreases to one quarter of its previous value. This implies that the size of the new domain is  $111 \times 41$ , i.e. 111 and 41 grid points in the x- and y-directions, respectively. Both Figure 3.4 and Figure 4.16 can be analyzed together to get a global view of the modifications made to the computational domain.

Due to the clustering, the grid spacing in both directions is reduced considerably in some regions of the domain, which has direct implications on the choice of the time step size in order not to violate the stability conditions of the scheme presented in (3.2). By using very small time steps, the stability issues of the scheme are avoided. Nevertheless, the smaller the  $\Delta t$  gets the longer the simulation takes. Therefore, it is convenient to be careful with the choice of the time step size to get a stable solution for as low computational costs as possible.

For the simulation of test case CFD1 using the new grid, the non-dimensional time step selected is  $\Delta t=0.00015$ . Once the simulation is done, the results obtained are the following for the time history of lift and drag coefficients, cf. Figure 4.17.

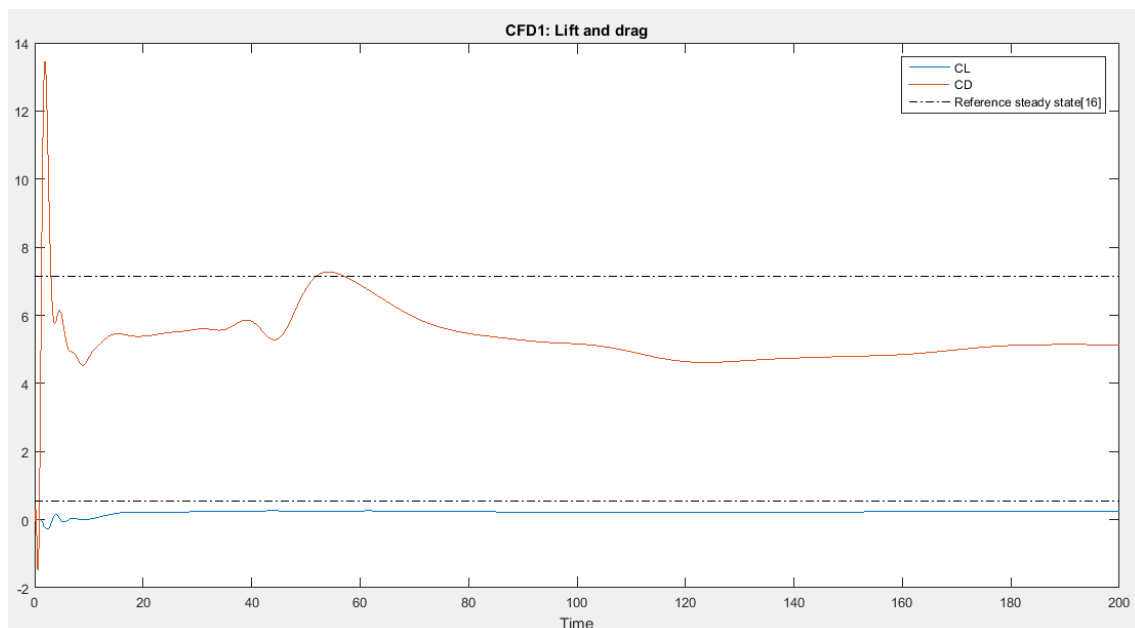


**Figure 4.17.** CFD1: Clustered grid

The results presented in Figure 4.17 show that the use of the new grid alleviates the problems mentioned for the equidistant grid, but the solutions for the lift and drag coefficients are still not accurate enough compared to the reference steady state solutions, represented by the dashed lines.

In order to analyze in detail the results obtained from the fluid solver, the following plots show the distribution of different physical quantities over the whole domain at the last time step of the simulation.

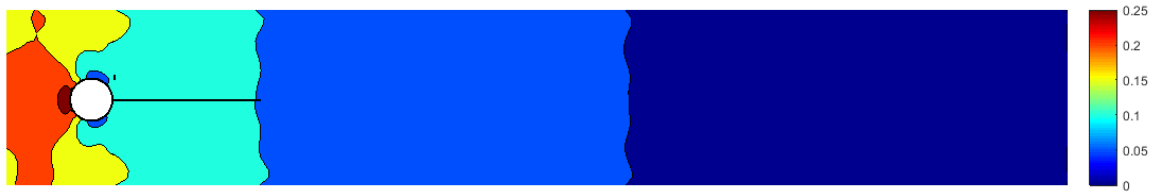


**Figure 4.18.** CFD1: Pressure distribution

It is important to remind that the solutions obtained from the fluid solver are in a non-dimensional perturbation form. As expected, Figure 4.18 shows how the maximum value for the gauge pressure takes place in the left side zone close to the cylinder, since its leading edge is a stagnation point. The pressure starts decreasing from there along the cylinder surface due to the flow acceleration there. It is also shown how the pressure is reduced when approaching the end of the channel to respect the zero gauge pressure condition at the outlet.

In order to focus the analysis on the surroundings of the structure, Figure 4.19 presents the non-dimensional gauge pressure profile along the cylinder surface. The mentioned pressure is defined in (4.7):

$$p - p_0 = \frac{p^* - p_0^*}{\rho_0^* (c_0^*)^2} \quad (4.7)$$

The superscript \* in (4.7) denotes dimensional quantities and the subscript 0 refers to stagnation values.

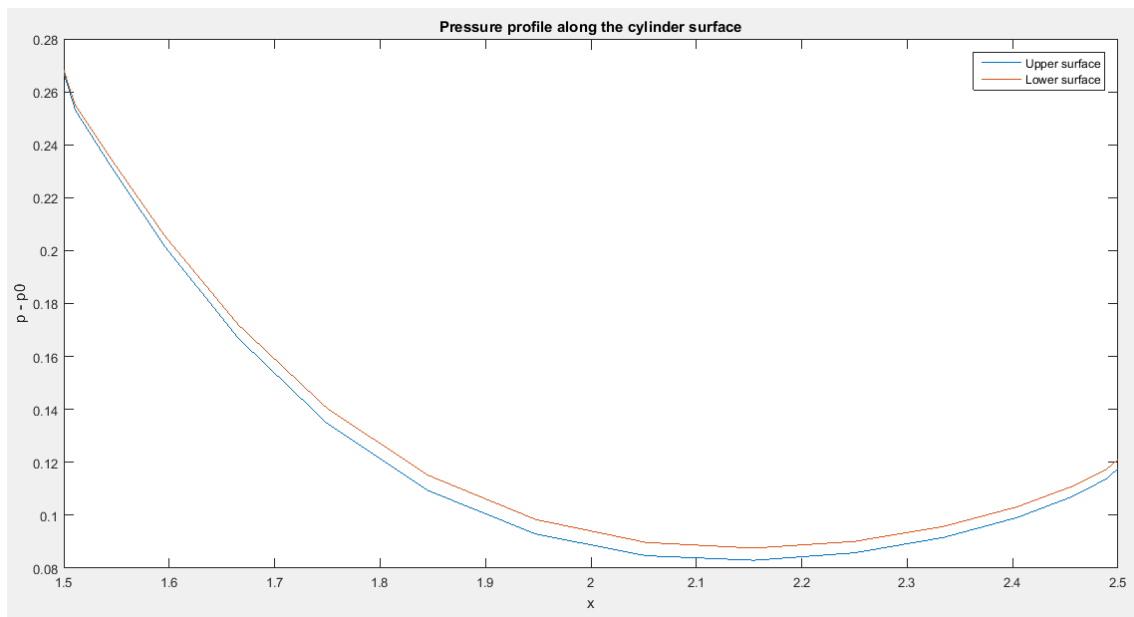


**Figure 4.19.** CFD1: Pressure profile along the cylinder surface

It is possible to observe in Figure 4.19 the difference in value between the pressure along the lower and upper surfaces represented by the red and blue lines, respectively. The lower pressure along the upper surface produces the suction to generate the lift force.

With regard to the flow velocity, Figure 4.20 gives the distribution of its horizontal component in a non-dimensional perturbation form at the whole domain, also for the last time step of the simulation.

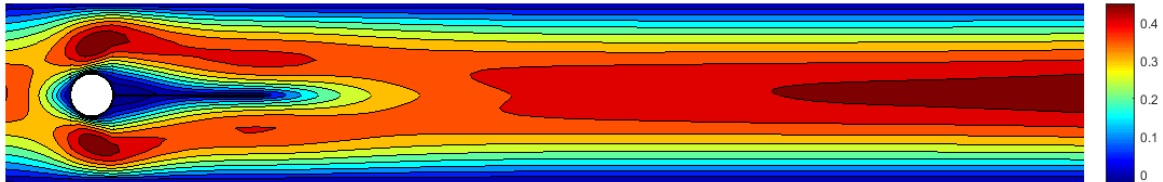


**Figure 4.20.** CFD1: Horizontal velocity distribution  $\left(u = \frac{u^*}{c_0^*}\right)$

Figure 4.20 shows the acceleration of the flow surrounding the cylinder in concordance with its pressure distribution presented in 4.19. The acceleration is bigger above the cylinder as it could be deduced from Figure 4.19. It is also possible to see how the horizontal velocity goes to zero at the channel walls and the fluid-structure interface to respect the no-slip boundary conditions. The parabolic velocity profile can be observed at the inlet following the specified boundary condition. Moreover, the velocity is shown to go up near outflow.

Finally another plot is added to give some information about the z-component  $w_z$  of the vorticity, over the entire computational domain, cf. Figure 4.21. The definition of  $w_z$  is given in (4.8).

$$w_z = (\nabla \times \mathbf{u})_z = \frac{\partial v}{\partial x} - \frac{\partial u}{\partial y} \quad (4.8)$$

In (4.8)  $\mathbf{u}$  is the velocity vector, while  $u$  and  $v$  refer to its horizontal and vertical components, respectively.



**Figure 4.21.** CFD1: Vorticity distribution

In Figure 4.21,  $w_z$  above the body is shown to be negative, while it is positive below it. Moreover, it is possible to see some kinks right at the boundaries of the blocks containing the cylinder. This indicates that the grid is non-smooth in those zones.

After this analysis, it seems that the fluid solver simulations do reflect correct physical phenomena. However, as it was mentioned before, the numerical results do not show high accuracy compared to the reference given in the benchmark.

In order to analyze the time step size choice, one more simulation is carried out using a different value for the non-dimensional  $\Delta t$ . The numerical results for lift and drag obtained in both simulations are presented in Table 4.13

**Table 4.13.** CFD1: Time step influence

	Drag and lift coefficients	
	CD	CL
$\Delta t=0,00025$	3,407	0,209
$\Delta t=0,00015$	5,138	0,234
<b>Reference</b>	7,145	0,560

By looking at the results shown in Table 4.13, the lack of accuracy is confirmed as none of the relative errors is lower than a 30%. In Table 4.13, the reference results are the ones computed in Table 4.12 as the non-dimensional values of the reference results given in Table 4.11. Nevertheless, the most important implication of Table 4.13 is that there is a time step influence on the results, which should not happen since the test case CFD1 represents a steady state. Therefore, even if this grid leads to better results than the equidistant one, the steady state solution is not being reached yet.

Two alternatives are considered at this point in order to solve the grid problems that seem to remain. The first one consists on a drastic modification of the grid surrounding the structure by using another grid type. A possible choice could be an O-grid where some grid lines would surround the whole body at increasing distances, while other grid lines starting at the surface of the body would cross them in locally perpendicular directions.

Despite the increase in smoothness of this kind of grid near the structure, other issues would appear when trying to match the last grid lines to the walls of the channel and to the vertical boundaries of the rest of unchanged blocks. Furthermore, it would be necessary to rewrite the code for the grid creation. So there are several reasons to turn this possibility down.

The second alternative is to keep the type of clustered grid unchanged while increasing the number of grid points in both directions. The low number of grid points along the cylinder surface of the current grid might explain the lack of accuracy of the results, so a grid refinement could be the solution. Moreover, by looking carefully at Figure 4.19, Figure 4.20 and Figure 4.21 some discontinuities can be noticed right at the leading and trailing edges of the cylinder. Therefore, it is possible that the current grid is just too coarse, and the grid problems could be alleviated with the mentioned grid refinement.

Hence, the number of grid points is doubled in both x and y directions leading to a finer grid. The modified number of grid points in the vertical direction is 41 for all the blocks. The modified numbers of grid points in the horizontal direction, considering the four columns of blocks starting from the left are 29, 31, 69 and 95, respectively. Then the size of the refined grid is 221 x 81, i.e. 221 and 81 grid points in the x- and y-directions, respectively.

The  $\beta$  parameters in (4.5) and (4.6) require a new study in order to select them properly for the refined grid. For the three vertical (considering the whole channel height) inter-block

boundaries from left to right, the values of the  $\beta$  parameter are 1.0086, 1.0098 and 1.5208. The  $\beta$  parameter used for the clustering in the y-direction is unchanged, with a value of 1.1.

After the mentioned modifications are carried out, the resulting grid is obtained and shown in Figure 4.22.

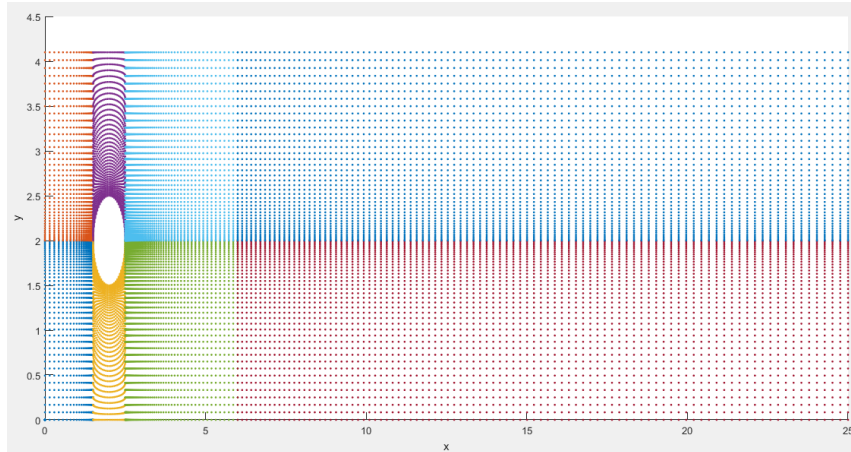


**Figure 4.22.** Computational domain using refined grid clustering

The changes on the new grid with respect to the previous one can be noticed by comparing Figure 4.16 and Figure 4.22. The high concentration of grid points shown in the surroundings of the cylinder and the first half of the flexible structure should, at least, improve the accuracy of the fluid solver results.

Nevertheless and as it was explained before, the big reduction on the grid spacing has direct implications on the time step needed to respect the stability conditions presented in (3.2). For the simulation of this test case using this refined grid, the method only accepts non-dimensional time steps smaller than  $\Delta t=10^{-5}$ , and the end time of the simulation should be around 200 to reach the steady state. Moreover, due to the doubling of the number of grid points in both directions, now the number of operations is multiplied by four at every time step. In other words, the simulations get extremely long.

After a few unsuccessful trials, it is confirmed that the current computational capacity level is not high enough to get solutions in reasonable times. Therefore, a higher computer performance is required in order to obtain reliable results from those simulations, and to be able to finish the validation of the fluid solver by comparison with the benchmark reference results.

#### 4.2.2. CFD2

The only fluid parameter that needs to be changed in the method from the ones used in test case CFD1 is the Reynolds number, which is set to be 100 as specified in Table 4.10. The rest of the fluid parameters (Mach number, Prandtl number etc) are unchanged to be coherent with the assumptions made at the beginning of the CFD Tests section.

Aiming to confirm the need for higher computer performance, the too coarse grid presented in Figure 4.16 is used as in test case CFD1, to see if the lack of accuracy in the results is evident again. In this case, the non-dimensional time step used is equal to 0.005 in order not to violate the stability conditions of the scheme.

The reference results after a grid refinement study are given in Table 4.14, which is directly taken from [16]. As explained before, these reference results have to be made non-dimensional by the use of (4.2) in order to be comparable, and such non-dimensional reference results are computed in Table 4.15.

**Table 4.14.** CFD2: Reference results (Table from [16])

level	nel	ndof	drag	lift
0 + 0	144	3032	$1.33188 \times 10^{+02}$	$1.18522 \times 10^{+01}$
1 + 0	576	11536	$1.34996 \times 10^{+02}$	$1.10739 \times 10^{+01}$
2 + 0	2304	44960	$1.36355 \times 10^{+02}$	$1.05337 \times 10^{+01}$
3 + 0	9216	177472	$1.36610 \times 10^{+02}$	$1.05303 \times 10^{+01}$
4 + 0	36864	705152	$1.36678 \times 10^{+02}$	$1.05347 \times 10^{+01}$
5 + 0	147456	2811136	$1.36696 \times 10^{+02}$	$1.05349 \times 10^{+01}$
5 + 1	150528	2869504	$1.36700 \times 10^{+02}$	$1.05346 \times 10^{+01}$
5 + 2	156672	2986240	$1.36701 \times 10^{+02}$	$1.05343 \times 10^{+01}$
5 + 3	168960	3219712	$1.36701 \times 10^{+02}$	$1.05340 \times 10^{+01}$
6 + 0	589824	11225600	$1.36700 \times 10^{+02}$	$1.05343 \times 10^{+01}$
ref.			136.7	10.53

**Table 4.15** CFD2: Non-dimensional reference results

	Drag and lift coefficients	
	CD	CL
Reference	2,734	0,211

The obtained results are shown in Figure 4.23.

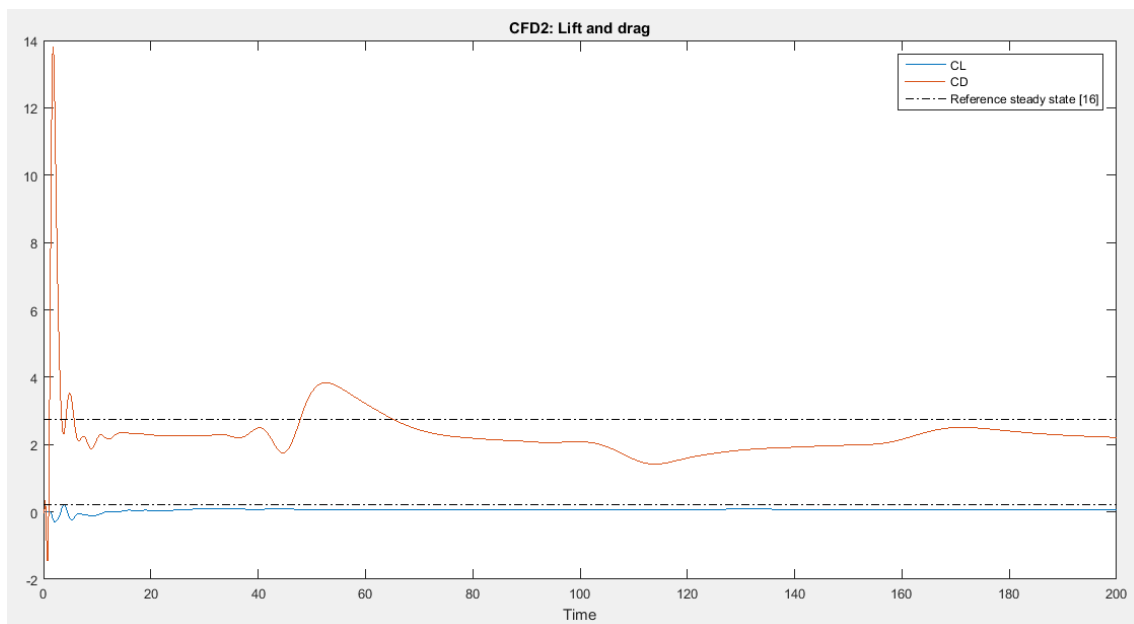


**Figure 4.23.** CFD2: Clustered grid

The numerical results from the fluid solver are presented in Table 4.16 together with the reference ones.

**Table 4.16.** CFD2: Numerical results

	Drag and lift coefficients	
	CD	CL
$\Delta t=0,0005$	2,211	0,065
<b>Reference</b>	2,734	0,211

As expected, the comparison shows that the fluid solver results approach the reference ones, but there is a lack of accuracy that leads to a relative error of 20% for the drag coefficient and even higher for the lift coefficient. As explained in test case CFD1, a higher computer performance should solve these problems of accuracy.

#### 4.2.3. CFD3

The last of the fluid dynamics test cases describes a time dependent state. The increase of the Reynolds number up to 200, shown in Table 4.10, gives rise to a change in the solution from the steady state already seen in CFD1 and CFD2 to stable oscillations. The assumptions made for the Mach number and the rest of the fluid parameters are the same as in the two previous test cases.

In order to analyze if the lack of accuracy already seen in the other tests gets bigger for a time dependent solution, the same coarse clustered grid from Figure 4.16 is utilized. In this case the stability conditions in (3.2) force the time step to be smaller than 0.002.

The development in time of the reference results is described in [16] by Table 4.17, where both a grid refinement and a time step study are done.

**Table 4.17.** CFD3: Reference results for  $\Delta t=0.01$  s and  $\Delta t=0.005$  s (Table from [16])

level	nel	ndof	drag	lift
1 + 0	576	11536	$416.8 \pm 3.3578[4.3825]$	$-24.702 \pm 342.38[4.3825]$
2 + 0	2304	44960	$437.29 \pm 5.3462[4.3825]$	$-11.085 \pm 429.88[4.3825]$
3 + 0	9216	177472	$438.99 \pm 5.4419[4.3825]$	$-10.289 \pm 433.09[4.3825]$
4 + 0	36864	705152	$439.38 \pm 5.4639[4.3825]$	$-9.9868 \pm 434.79[4.3825]$
level	nel	ndof	drag	lift
1 + 0	576	11536	$416.83 \pm 3.4023[4.3956]$	$-23.897 \pm 346.72[4.3956]$
2 + 0	2304	44960	$437.41 \pm 5.5856[4.3956]$	$-12.673 \pm 434.74[4.3956]$
3 + 0	9216	177472	$439.05 \pm 5.5804[4.3956]$	$-11.837 \pm 436.17[4.3956]$
4 + 0	36864	705152	$439.45 \pm 5.6183[4.3956]$	$-11.893 \pm 437.81[4.3956]$
<b>ref.</b>			$439.45 \pm 5.6183[4.3956]$	$-11.893 \pm 437.81[4.3956]$

The reference mean values of the oscillations are made non-dimensional, obtaining values of 2.197 and -0.059 for the drag and lift coefficients respectively.

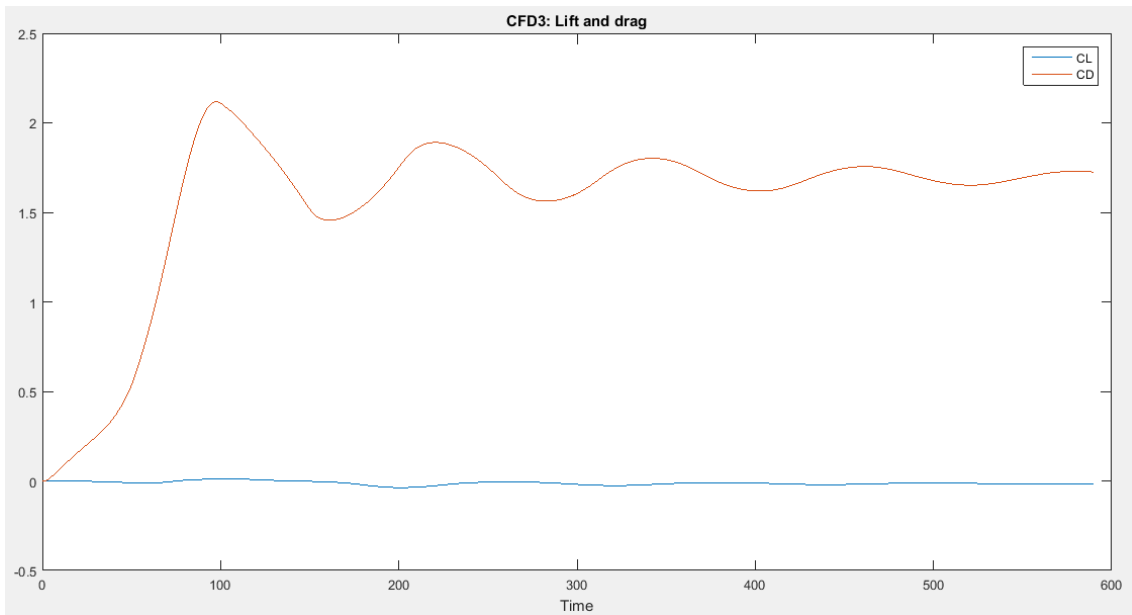


**Figure 4.24.** CFD3: Clustered grid

As shown in Figure 4.24, the flow results are poor. Apart from the repeated lack of accuracy in the mean values of lift and drag, the results obtained do not show the stable oscillations that are expected according to Table 4.17. Therefore, the grid problems discussed for CDF1 and CFD2 are even more evident for this case with a higher Reynolds number, so the need for higher computer performance is confirmed in order to get better results.

### 4.3. FSI Tests

This final section of the whole results chapter aims to validate the existing method itself, unlike the two previous parts where both the structure and the fluid solvers of the method were studied separately. Therefore, the FSI test cases must take into account the fluid-structure interaction and analyze its effects on the structure and fluid dynamics.

All the assumptions made for the fluid and structural parts apply in this section as well, in order to be consistent with the results already obtained. Hence, for the FSI test cases an infinitely thin flexible structure is submerged in an air flow.

It is important to remind that the existing method uses the governing equations of fluid and structure in a non-dimensional formulation. Therefore, the differences of the benchmark configuration should not affect the results if the non-dimensional input parameters are appropriately selected to achieve an equivalent case.

For the FSI tests the ratio between the fluid and structure densities is specified in the benchmark, so this quantity must be conserved by the parameters used in the method. As the

density of air is known, this ratio gives the appropriate density of the flexible structure  $\rho^s$  for the method.

The non-dimensional governing equation for the structure used in the method can be divided by the non-dimensional specific mass of the plate:

$$\ddot{w} + \frac{B}{M} w_{xxxx} = \frac{-\Delta p}{M} \quad (4.9)$$

In the resultant equation (4.9), the ratio between the non-dimensional flexural rigidity and specific mass of the flexible structure is the quantity that must be matched to the same ratio computed for the benchmark values, in order to get equivalent cases.

$$\frac{B}{M} = \frac{\tilde{B}}{\tilde{M}} \Big|_{\text{Benchmark}} \quad (4.10)$$

Since the  $\rho^s$  is now known, the M can be computed by using (2.13) and making the result non-dimensional. The right hand side of (4.10) can be calculated with the values given in the benchmark, and its multiplication by the just computed M gives the appropriate value of B. The use of these input parameters in the existing method leads to FSI test cases which are equivalent to those described in the benchmark in Table 4.18 [16].

**Table 4.18.** Parameter setting for the FSI tests (Table from [16])

parameter	FSI1	FSI2	FSI3
$\beta = \frac{\rho^s}{\rho^f}$	1	10	1
$\nu^s$	0.4	0.4	0.4
$Ae = \frac{E^s}{\rho^f U^2}$	$3.5 \times 10^4$	$1.4 \times 10^3$	$1.4 \times 10^3$
$\rho^f [10^3 \frac{\text{kg}}{\text{m}^3}]$	1	1	1
$Re = \frac{U d}{\nu^f}$	20	100	200
$\bar{U} [\frac{\text{m}}{\text{s}}]$	0.2	1	2

The settings described in Table 4.18 lead to a steady state solution for the test case FSI1 and to periodic solutions for FSI2 and FSI3.

In order to get coherent results from the simulation of all these FSI test cases, a very precise coordination among fluid and structure solvers is required, so both of them must show a correct and accurate performance.

Therefore, the end of the validation process of the present FSI method can only be reached once the problems of accuracy of the fluid part are solved.

## 5. Conclusions and outlook

The purpose of this final section is to explain the main conclusions derived from the development of the project work. In addition, an outlook for further investigation is presented.

### 5.1. Conclusions

According to the title of the specialization project, an in-depth investigation of the FSI method has been carried out. The separate analyses of both the structure and fluid solvers provided the necessary results to draw some conclusions.

In relation to the structural part, it is clear that the 1D simplification of the structure movement has an important influence on the results. By neglecting the horizontal displacement of the plate, the vertical one gets slightly bigger and so does the corresponding oscillation period. When comparing with the reference results, the low relative errors obtained are acceptable, taking into account the lower number of grid points used along the structure. The FSI method adopts the Euler-Bernoulli beam model for the structure, which is considered infinitely thin in the domain discretization. Nevertheless, in the benchmark the flexible structure has a finite thickness and it is modeled by giving its Cauchy stress tensor by the constitutive law for St. Venant-Kirchhoff material. Despite those simplifications and differences, by looking at the comparison of results, it is reasonable to consider them as valid.

When studying the fluid part, several assumptions are made for the fluid flow. Since the existing method is originally created to work with gases, the fluid is considered to be air instead of glycerine as specified in the benchmark. Moreover, the compressible Navier-Stokes equations are adopted in the FSI method unlike in the computation by Turek and Hron [16], where they are incompressible. By choosing the appropriate non-dimensional fluid parameters and keeping the Mach number low, the tendency of the results for all simulations looks correct. Nevertheless, the obtained relative errors are not low enough. This lack of accuracy of the results is due to grid problems near the grid lines in the  $y$ -direction through the leading and trailing edges of the cylinder. Either a change of grid type or a substantial grid refinement is needed in order to improve the accuracy of the results.

The correct and precise performance of the whole FSI method is equally dependent on both the fluid and the structure solvers. Therefore, the complete validation of the method cannot be achieved until the accuracy problems shown in the fluid part are solved.

### 5.2. Outlook

As an outlook and regarding the conclusions, further development of this project work should focus first on improving the accuracy of the fluid solver results. For doing so, two possibilities were proposed when discussing the results.

On the one hand, the use of an O-grid in part of the computational domain can be expected to alleviate the grid problems in the surroundings of the structure. This possibility requires re-writing the part of the original code where the grid is created. Moreover, the grid discontinuities move now to the walls of the channel which might affect the correct definition of the boundary conditions there.

On the other hand, a full grid refinement study can be done to analyze if the lack of accuracy is due to discontinuities at the leading edge of the structure or if it is just a matter of a too coarse grid. The challenge with this possibility is now related to computational costs, so a relatively high computer performance is needed.

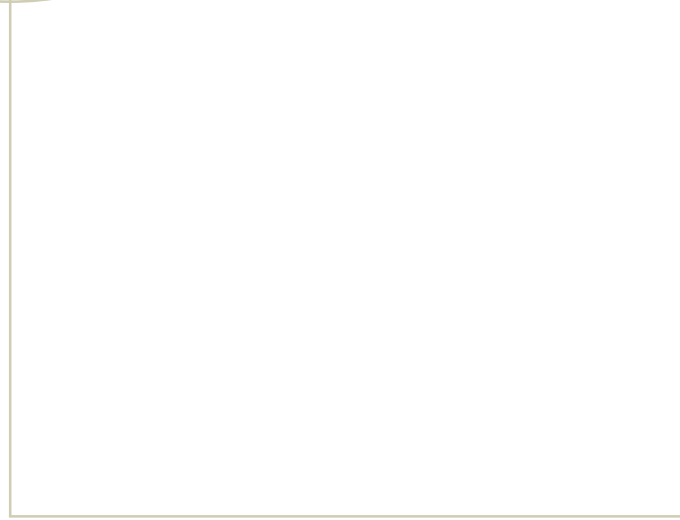
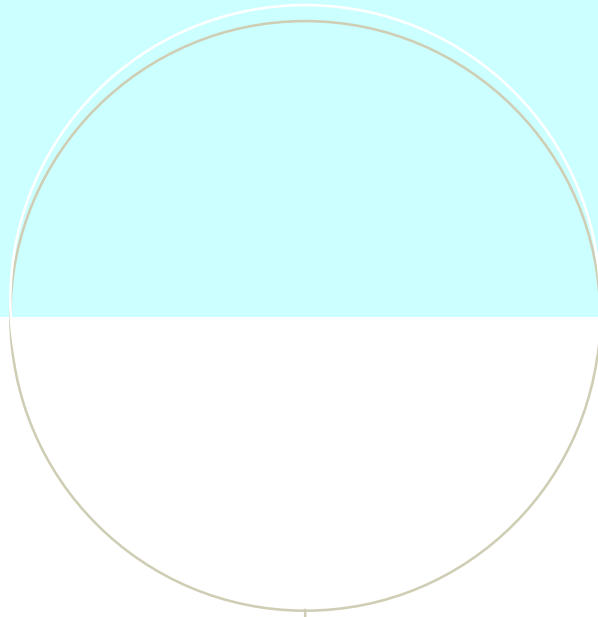
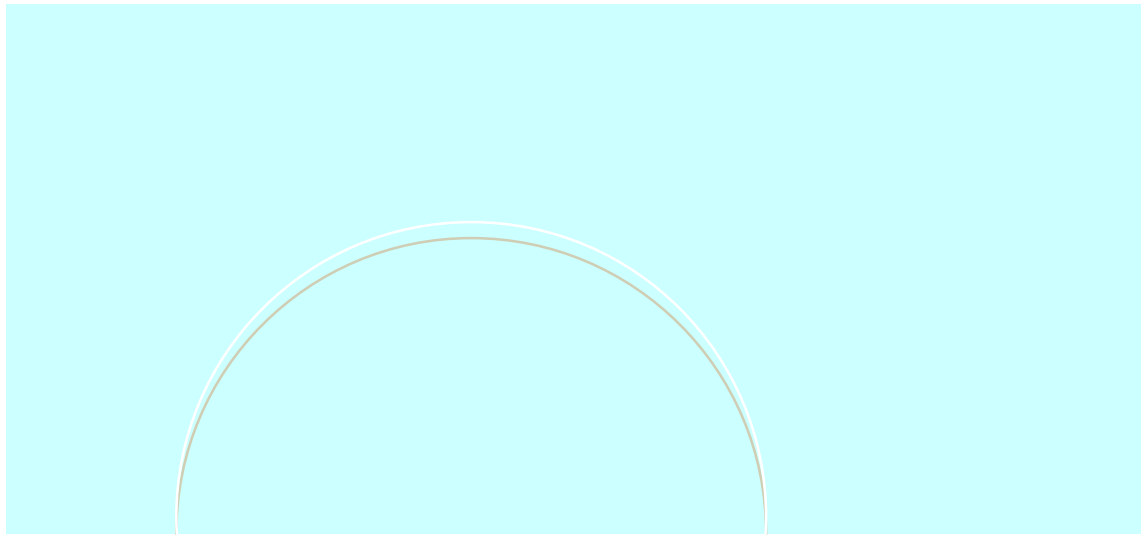
Once the problems are solved, the following steps involve simulating correctly the FSI test cases and then the validation of the method can be completed.

To sum up, some improvements of the method could be carried out in relation to the inter-block communication mechanism. The grid problems caused by the jumps in cell sizes and angles might be alleviated by a reduction of the inter-block communication. The idea is to stop using ghost points at the block boundaries where the communication is allowed, in order to avoid computing across points with big differences in grid spacings on both sides. The points at the block boundaries are considered as belonging to both blocks, allowing each of them to have information about the other and maintaining the current communication.

## References

- [1] Modeling of Obstructive Sleep Apnea by Fluid-Structure Interaction in the Upper Airways (OSAS Mod) project website: <http://osas.no/>
- [2] H.-J. Bungartz and M. Schäfer (eds.). Fluid-structure Interaction: Modelling, Simulation, Optimization. Springer-Verlag, 2006.
- [3] J.F. Sigrist. Fluid-Structure Interaction: An Introduction to Finite Element Coupling. Wiley, 2015.
- [4] American Academy of Sleep Medicine. International Classification of Sleep Disorders, revised: Diagnostic and Coding Manual. Chicago, Illinois: American Academy of Sleep Medicine, 2001.
- [5] Osborne Head&Neck Institute website: <http://www.ohniww.org/>
- [6] M. Khalili, M. Larsson and B. Müller. Interaction between a Simplified Soft Palate and Compressible Viscous Flow. Submitted 2016.
- [7] B. Müller. Governing Equations of Compressible Fluid Flow. Lecture Notes of NGSSC CFD Course, Uppsala University, 2003.
- [8] R. H. Pletcher, J. C. Tannehill and D. A. Anderson. Computational Fluid Mechanics and Heat Transfer. CRC Press, 3rd ed., 2012.
- [9] M. Larsson. Numerical Modeling of Fluid-Structure Interaction in the Human Larynx. PhD Thesis, No. 2010:155, Faculty of Engineering Science and Technology, Norwegian University of Science and Technology, Trondheim, Norway, 2010.
- [10] T.S. Balint and A.D. Lucey. Instability of a Cantilevered Flexible Plate in Viscous Channel Flow. Journal of Fluids and Structures, 20 893–912, 2005.
- [11] M. Khalili, M. Larsson and B. Müller. Numerical Simulation of Fluid-Structure Interaction for a Simplified Model of the Soft Palate. Coupled Problems, San Servolo Island, Venice, Italy, 2015.
- [12] M.R. Visbal and D.V. Gaitonde. On the Use of Higher-Order Finite-Difference Schemes on Curvilinear and Deforming Meshes. J. C Phys., 2002.
- [13] A. Kalmbach and M. Breuer. Investigations on Fluid-Structure Interactions using Volumetric Particle-Image Velocimetry. 16th Int. Symp. on Applications of Laser Techniques to Fluid Mechanics. Lisbon, Portugal, 2012.
- [14] J. P. Gomes and H. Lienhart. Experimental Benchmark: Self-Excited Fluid-Structure Interaction Test Cases. H.-J. Bungartz et al. (eds.), Fluid Structure Interaction II, Lecture Notes in Computational Science and Engineering 73. Springer-Verlag, Berlin Heidelberg, 2010.

- [15] C. C. Wong. Experimental Study of Fluid Structure Interaction Effects on Metal Plates under Fully Developed Laminar Flow (Master's Thesis). Naval Postgraduate School, Monterey CA, 2011.
- [16] S. Turek and J. Hron. Proposal for Numerical Benchmarking of Fluid-Structure Interaction between an Elastic Object and Laminar Incompressible Flow. In H. Bungartz and M. Schäfer, editors, Fluid-Structure Interaction: Modelling, Simulation, Optimisation, LNCSE-53. Springer, 2006.
- [17] B. Müller. Methods for Euler and Navier-Stokes Equations. Lecture Notes of NGSSC CFD Course, Uppsala University, 2003.
- [18] N. M. Newmark. A Method of Computation for Structural Dynamics. Journal of the Engineering Mechanics Division 85, 67-94, 1959.
- [19] H. Hashamdar, Z. Ibrahim and M. Jameel. Finite Element Analysis of Nonlinear Structures with Newmark Method. International Journal of the Physical Sciences Vol. 6(6), 1395-1403, 2011.
- [20] G. O. Roberts. Computational Meshes for Boundary Layer Problems. Proc. 2nd Int. Conf. on Numerical Methods in Fluid Dynamics. Lecture Notes in Physics, Vol. 8, Springer-Verlag, Berlin, 171-177, 1971.



**NTNU – Trondheim**  
Norwegian University of  
Science and Technology